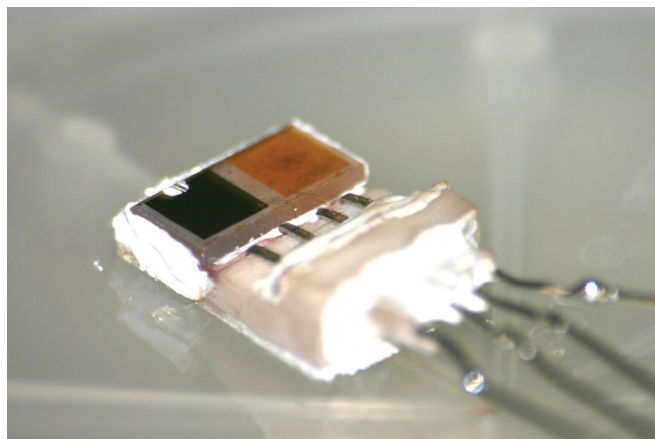


Thin film potentiometric NO_x sensor by Pulsed Laser Deposition



Master thesis of W.B.J. Baake, s0011142

Enschede, 14-1-2007

Chemical Engineering
Inorganic Materials Science
Faculty of Science & Technology
University of Twente

Graduation committee:

Chairman:	Prof. Dr. Ing. D.H.A. Blank
Mentor:	Dr. Ing. A.J.H.M. Rijnders
CT-i mentor:	Dr. B.A. Boukamp
Members:	Dr. H. Schönherr
	Ir. F. Vroegindeweyj

Abstract

Nitrogen oxides (NO_x) are considered harmful gases because of their contribution to acid precipitation, smog formation and their roles as greenhouse gases. The main NO_x emission come from combustion processes (for instance in automobiles). Strategies are developed to combat NO_x emissions but the absence of means to detect NO_x concentrations selectively, fast, cost-effectively and in a fast way is hindering effective usage of these emission-control strategies.

Potentiometric NO_x sensor have shown potency to fulfill this detection role in automotive and other environments. Most sensors rely on stabilized zirconia electrolytes that have high ionic conductivity and a suitable combination of electrodes to produce an electric potential across the electrodes that is a function of NO_x concentration.

Nanotechnology is based on the premise that materials obtain interestingly different characteristics at small length scales compared to bulk materials. Therefore, it is interesting to investigate the behavior of NO_x sensors with thin film electrodes. Deposition is done by means of Pulsed Laser Deposition (PLD) in this research.

ZnFe₂O₄ and NiO have been identified as suitable sensing electrode materials based on literature. These have been combined with a Pt reference electrode to form a NO_x sensor.

Pt electrodes have been deposited at different pressures and target-substrate distances (d_{t-s}) in an attempt to obtain porous films, suited as electrodes. Deposition at pressures above 1 mbar yielded porous layers for all used d_{t-s} . Poor adhesion of these porous layers to the substrate render them unsuitable for actual sensor applications however.

The effect of an increase of deposition temperature of ZnFe₂O₄ layers on their microstructure and crystallinity was found. At room temperature no cubic ZnFe₂O₄ was deposited and layers seemed dense. Deposition at 300 °C showed some cubic phase and columnar growth behavior. Deposition at 300 °C showed more cubic phase and a dense layer with larger grains than at room temperature.

Annealing of ZnFe₂O₄ layer deposited at room temperatures showed no change in crystallinity up to 900 °C and the emergence of Fe₂O₃ and Fe₃O₄ phases at 1200 °C. After annealing at 1200 °C the thin film had transformed into smaller islands on the substrate.

A gas flow setup for the characterization was built, automated and characterized in terms of delay time and transition time for changes in gas composition. A delay time of 10s and a transition time of 3.4s were determined for a total gas flow rate of 150 ml/min.

Two sensors were characterized and showed a positive response to increasing concentrations of NO₂. This response could not be fitted with linear or logarithmic functions. O₂ cross-sensitivity at 200 ppm NO₂ were determined for both sensors. Response time could not be determined adequately at the used measurement protocol. Comparison with literature therefore remained difficult.

Acknowledgments

No work of any significance can be done without the help of others, whether it is directly or indirectly related to the work. I consider myself quite lucky with the co-workers, friends and loved ones that have been in my life over the last couple of years and especially during the last year. Therefore, I would like to use this chapter to mention and thank several of them individually. Of course it is true that for every one person you mention you will forget many others, so to them I would like to apologize up front.

When I think of my period in the IMS group the first person that comes to mind is Professor Dave. Even after mild insults during the study tour in South Africa he still provided me with the opportunity to go to Stanford University for my internship. His enthusiasm for nanotechnology, his good care for students and his generosity inspired me from the moment we met.

Guus I would like to thank for his good advices, excellent discussions and sharing a love for gadgets, technology and winter sports.

To Frank! I am grateful because of his good support, guidance and patience as a mentor and for teaching me the difference between Zeeland and Zuid-Holland.

Many problems in the lab I could not have overcome with the help of Henk Veldhuis and Frank Roesthuis who saved me several times when I had to make or fix something and did not go crazy even if I bugged them ten times a day.

Matthijn and Paul have taken their time to teach me how to work the equipment in the thin film lab without which I could not have done this research.

I thank all the members of the IMS group for providing a great atmosphere to work in, during work hours and at other activities.

Six and a half years in Enschede yielded me a magnificent group of friends with whom I have had great times. A reunion in 2010 is already in the making for all the friend from Chemical Engineering, but I do hope we stay in touch before that and after.

A special thanks should go out to Raymon, Lodewijk and Bart, who provided good conversation and laughter during lunchtime, work, squashing, etc...

Some days in the year could just not be spent toiling away at research while a fierce wind was blowing. Those were the days I changed my "lab coat" for a wetsuit and tried to tame wind and waves together with the dudes and chicks from Hardboard, the wind- and kite surf association. Because there ain't no party like a Hardboard party!

A big thanks for all the people who have lived together with me at "Huize Antonio" for the past three years. It was great living with you!

However, none of this all would have been possible without the unconditional love and support from my parents. Thank you for providing me with so many opportunities!

Finally I would like to thank Verena. You make each day a bit brighter.

Table of Contents

ABSTRACT	1
ACKNOWLEDGMENTS	3
TABLE OF CONTENTS	5
1. INTRODUCTION	7
1.1. OBJECTIVE	8
2. THEORETICAL BACKGROUND	9
2.1. TYPES OF SOLID STATE NO _x SENSORS	9
2.2. SENSOR GEOMETRIES	9
2.3. PREVIOUS RESEARCH.....	11
2.4. IONIC CONDUCTIVITY IN STABILIZED ZIRCONIA.....	12
2.5. ELECTROMOTIVE FORCE	14
2.6. NON-NERNSTIAN BEHAVIOR	18
2.7. ELECTRODES.....	22
2.8. PULSED LASER DEPOSITION.....	24
2.9. ELECTRODE PATTERNING TECHNIQUES	26
3. EXPERIMENTAL	29
3.1. ELECTRODE DEPOSITION	29
3.2. PATTERNING OF THE ELECTRODES	33
3.3. ELECTRODE ANALYSIS	34
3.4. GAS FLOW MEASUREMENTS	35
4. GAS FLOW SETUP CONTROL SOFTWARE DESIGN	39
4.1. REQUIREMENTS.....	39
4.2. ENVIRONMENTAL MODEL.....	40
4.3. DATA FLOW DIAGRAM FOR PROCESSES	40
5. RESULTS	43
5.1. ZNFe ₂ O ₄ ELECTRODES	43
5.2. PT ELECTRODES	50
5.3. GAS FLOW SETUP	54
5.4. SENSORS	56
6. DISCUSSION	61
6.1. ELECTRODES.....	61
6.2. GAS FLOW SETUP	63
6.3. SENSORS	64
7. CONCLUSION	67
8. RECOMMENDATIONS	69
8.1. ELECTRODES.....	69
8.2. GAS FLOW SETUP	69
8.3. SENSORS	70
9. REFERENCES	71
10. LIST OF ABBREVIATIONS	73
11. LIST OF SYMBOLS	75
APPENDIX A: SEM IMAGES OF PT LAYERS	77

1. Introduction

Over the last decades awareness has grown that we as mankind can severely influence the environment in which we live. Together with this awareness comes the realization that in these few decades the growth of the earth's population and general level of wealth has caused several complicated problems. Among the problems that are commonly accepted as being caused by mankind are the depletion of the ozone layer, global warming and acid precipitation.

Acid precipitations are a serious threat to many ecosystems as well as to sandstone structures, which erode more quickly due to acid rain. Surface waters become more acidic, causing fish and insects to die. Soils acidify, which kills certain types of microbes, leaches away nutrients and minerals from the top soil and mobilizes toxins. Acid precipitation is caused by gas phase reactions of sulfur dioxide or nitrogen oxide (NO_x) with hydroxyl radicals available in the air, resulting in sulfuric acid and nitric acid.

Nitrogen oxide (NO_x) is a general term that is applied to a multitude of oxides of nitrogen (from NO to N₂O₅) but is most commonly used to specify the total of nitrogen monoxide (NO) and nitrogen dioxide (NO₂). This definition for nitrogen oxide will be used throughout this report. Besides the earlier mentioned acid precipitation, nitrogen oxide is also a greenhouse gas and a contributor to smog formation.

Nitrogen oxide is formed primarily in combustion reactions when burning nitrogen containing fuels, where the nitrogen is released as a free radical, which is then able to react with the oxygen present in the combustion gases or the atmosphere. At elevated temperatures (above 1600 °C) nitrogen oxide can also be formed when using fuels that contain no nitrogen due to the reaction of nitrogen with oxygen radicals, oxygen with nitrogen radicals or nitrogen with hydroxyl radicals^[1].

The internal combustion engine is still the power source for all but a few road vehicles and as such can be a major contributor to the emission of nitrogen oxide. Since 1975 cars have been equipped with catalytic converters which convert harmful gases to less harmful ones. The most commonly applied type of catalytic converter is the three-way converter, which catalyses the oxidation of carbon monoxide and remnant fuel as well as the reduction of nitrogen oxides:

This kind of catalytic converter works best when the engine is working in stoichiometric conditions, that is when the air to fuel ratio is such that (in theory) all the oxygen in the air is used to burn the available fuel. For fuel that is equivalent to octane and at sea level this works out to a mass ratio of 14.7 to 1, air to fuel^[2]. If this air to fuel ratio differs from stoichiometry then there will be either unburned fuel or an excess of oxygen, leading to reducing or oxidizing conditions respectively. This decreases the efficiency of the catalyst towards either the oxidizing or reducing reactions and thereby increases harmful emissions.

As fuel prices rise and reducing carbon dioxide emissions becomes more important a greater emphasis is placed on fuel efficient engines. A particularly useful technique is the employment of so-called lean burn engines, in which far more air is admitted into

the engine than required for the combustion reaction, yielding a higher fuel efficiency due to higher compression ratios. This leads to an increase in oxygen content of the exhaust gases, which in turn halts the reduction of nitrogen oxide at the three way catalyst. Thus, the amount of nitrogen oxide emissions will be higher for these engines.

European regulations on NO_x emissions are becoming more and more strict every year as shown in Table 1. As a result car manufacturers have to find ways to reduce the emissions of their vehicles to keep them legal in the EU.

Table 1: European emission standards for HD diesel engines^[3]

Emission standard	Year	NO _x (g/kWh)
Euro III	2000	5
Euro IV	2005	3,5
Euro V	2008	2

To combat these NO_x emissions several solutions have been developed, which either limit the production of NO_x by lowering the engine temperature (through exhaust gas recirculation), convert NO_x in the exhaust fumes continuously (by adding a reduction agent such as ammonia or urea) or temporarily store NO_x and convert it batch wise.

The ideal solution would be to monitor NO_x concentrations in the exhaust gases – directly in the exhaust ports (in a closed-loop setup to minimize NO_x emission) *and* before and after the adsorbent (to determine if it is functioning as desired).

For this purpose the development of nitrogen oxide sensors becomes critical. Operating temperature and response time specifications differ for these two applications. A higher operating temperature and a fast response time is required for sensors in a closed loop engine management setup. Response time requirements are lower for sensors measuring adsorbent effectiveness, but they are required to operate at lower temperatures.

This research has focused on sensors suitable for adsorbent effectiveness monitoring.

Besides the application in the automotive industry a small, sensitive, durable and cost-effective nitrogen oxide sensor would be applicable in many other fields, such as industrial burners. Implementation in the automotive industry however is an extremely testing application as size restrictions, lifetime expectancy, ease of use and costs weigh heavily in this case. Solid state sensors could live up to these expectations.

1.1. Objective

The aim of this work is to create an NO_x-sensor that is sensitive to NO_x gas over a wide concentration range, insensitive to other species in the analyte gas (cross-sensitivity) and preferably has a fast response to changes in NO_x concentration. Operational temperatures are expected to lie between 400 °C and 800 °C. The electrodes are manufactured by using PLD technology to create thin film electrodes. Electrodes need to be characterized with respect to their composition and structure. Furthermore a system has to be developed which allows the sensors to be characterized. This characterization system is to be automated, so that measurements are easy to perform.

The characteristics of this sensor are to be compared to sensors that have electrodes which are manufactured with conventional powder based production techniques.

2. Theoretical background

In this chapter the theoretical background of the working principles of the sensor will be described, as well as the techniques that were used to manufacture the sensor.

Paragraph 2.4 discusses the origin of ionic conductivity in stabilized zirconia. The working principle of a potentiometric sensor is based on a change of the electromotive force, for which the theoretical background is explained in paragraph 2.5. In paragraph 2.6 non-Nernstian sensor behavior and the concept of mixed potential are investigated and a prediction for sensor response is made. In paragraph 2.7 the influence of the electrodes on the sensor behavior is elucidated, a fixed oxygen potential reference electrode is introduced and patterning methods for electrodes are discussed. Concluding this chapter is paragraph 2.8, in which the pulsed laser deposition technique is discussed that will be used to deposit the electrode materials.

2.1. Types of solid state NO_x sensors

Solid state NO_x sensors can roughly be divided into several categories^[4, 5]:

- Potentiometric
- Amperometric
- Resistive
- Impedance
- Acoustic

The first two types respectively generate a potential across or a current through an ion-conducting electrolyte whereas the latter three function on the basis of changing material properties as a function of NO_x concentration. This report will focus on potentiometric NO_x sensors as these are easier to manufacture than amperometric and acoustic sensors and easier to read out than sensors based on impedance.

Resistive sensors are quite sensitive to pollution of the surface, limiting their lifetime and therefore usability in automotive applications. It must be noticed however that their initial performance is rather good.

All potentiometric NO_x sensors are based on an ion-conducting electrolyte on which two or more electrodes are placed. Most of these use a stabilized zirconia electrolyte, which is zirconium dioxide which has been doped with yttria, scandia or calcia, thereby transitioning the zirconia from the monoclinic to the cubic phase and inducing oxygen vacancies - thereby giving the zirconia its oxygen conducting properties.

2.2. Sensor Geometries

Many groups have researched the possibilities of potentiometric nitrogen oxide sensors over the past years. Most of the research departs from the work on yttria stabilized zirconia (YSZ) oxygen sensors^[6] and thus much of the first research was done on tubular sensors, which consist of a single end closed tube of stabilized zirconia with electrodes on the inner and outer surface of this tube. The inner electrode is usually

exposed to a gas with a known composition, also known as a reference gas, thus this electrode is usually called the reference electrode.

The outer electrode then is exposed to a gas of which the concentration of certain species is of interest and thus that electrode is known as the sensing electrode.

An example of such a commonly used geometry is shown in Figure 1.

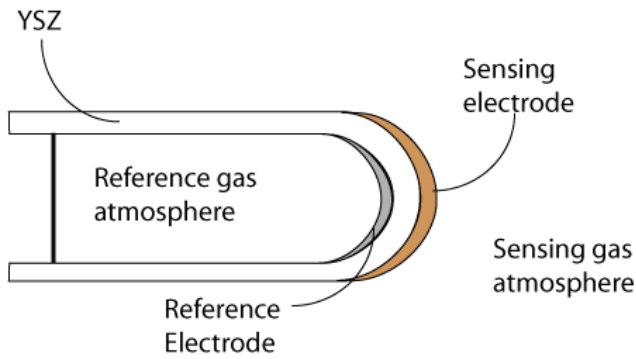


Figure 1: An example of a tubular sensor, side view

Commonly the reference electrode (RE) is exposed to a reference gas (usually air) which is sealed from the environment. A design incorporating a closed compartment is however very hard to realize with thin film techniques. A design for sensors based on thin layers is a flat substrate with electrodes on either side, as shown in Figure 2. The usage scenarios could be that either the entire sensor is exposed to the same gas environment or that the reference electrode is exposed to a reference gas and the sensing electrode (SE) is exposed to the target gas. However, this design also faces some practical drawbacks, as the sample has to be glued or clamped to the substrate holder in the deposition system, which will most likely damage the already deposited layer on the backside of the substrate.

Therefore, a third design is considered, again based on a flat substrate, but with both electrodes on one side, as shown in Figure 3.

Main advantages of this design are the ease of production and therefore low costs.

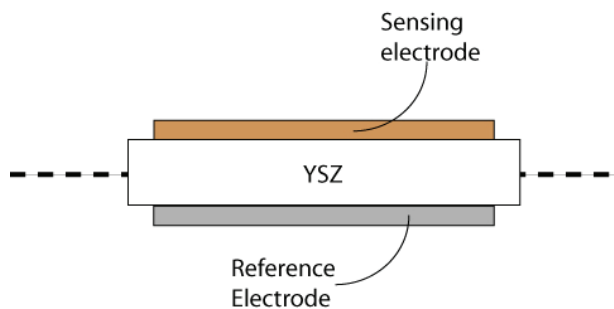


Figure 2: Example of a flat sensor, side view

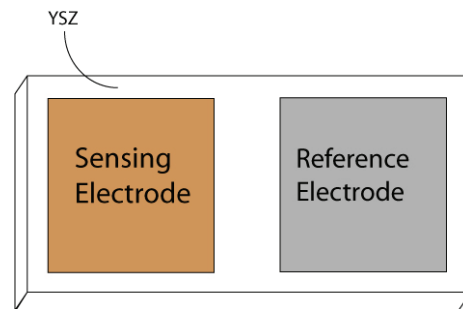


Figure 3: Example of a flat sensor with both electrode on one side, top view

2.3. Previous Research

The electrolyte material for potentiometric NO_x sensors is usually yttria stabilized zirconia (YSZ), as explained in paragraph 2.1. For bulk materials most characteristics are quite well known and therefore most of the research focuses on optimizing the electrode material, morphology and the overall sensor geometry.

Many materials have been tested as electrode materials, ranging from metals, via simple oxides (such as NiO and WO₃) to mixed oxides (spinel type oxides such as ZnFe₂O₄ as well as perovskite oxides such as LaFeO₃).

Zhuikov *et al* have published a review paper^[3] in which a summary is given of the oxide materials that had been used as sensing electrodes, as shown in Table 2. A report by Miura *et al.*^[7] shows the sensitivities of sensors equipped with different types of simple oxide sensing electrodes combined to a Pt reference electrode (kept in atmospheric air). Their results are summarized in Table 3.

Table 2: Typical examples of the SE materials for potentiometric mixed-potential type NO_x sensors reported by different authors^[3]

Oxide sensing electrode materials	Operating temperature (°C)	Measuring concentration (ppm)	Year of publication
WO ₃	500–700	5–200	2000
WO ₃	450–700	20–1000	2004, 2005
NiCr ₂ O ₄	550–650	15–500	2001–2004
ZnCr ₂ O ₄	550–650	20–500	2001–2005
ZnFe ₂ O ₄	550–700	20–500	2002–2005
ZnO	550–700	50–450	2004, 2005
Cr ₂ O ₃	500–600	100–800	1996, 2003, 2004
Cr ₂ O ₃ + oxidation catalyst	500–600	20–1000	2000–2005
NiO	700–900	50–400	2004, 2005
LaFeO ₃	450–700	20–1000	2001, 2004
La _{0.8} Sr _{0.2} FeO ₃	450–700	20–1000	2004
La _{0.85} Sr _{0.15} CrO ₃ /Pt	600–700	20–1500	2005
Tin-doped indium (ITO)	613	100–450	2005
La _{0.6} Sr _{0.4} Fe _{0.8} Co _{0.2} O ₃	500	100–600	2004
CuO+CuCr ₂ O ₄	518–659	10–500	2005

Table 3: EMF (ElectroMotive Force) values to 400 ppm NO₂ at 850 °C for the sensor using following single oxide SEs in dry air (21 vol.% O₂)^[7]

Sensing electrode	ΔEMF (mV)
NiO	40.7
SnO ₂	19.2
TiO ₂	16.8
Ga ₂ O ₃	11.0
Cr ₂ O ₃	8.9
ZnO	5.4
Nb ₂ O ₃	4.3
In ₂ O ₃	2.1
Co ₃ O ₄	0.4
Pt	0.1

A ΔEMF value of 52 mV was reported by Miura *et al.*^[8] for ZnFe₂O₄ in NO₂ at 700 °C

Based on these studies the materials chosen to use as electrodes in this research are ZnFe_2O_4 and NiO . These materials have shown to give a large response to NO_x .

Up to now, most of the electrodes were made by deposition of a layer of powder (usually in a suspension) on the electrolyte material and sintering the powder to form a more or less dense electrode. Thicknesses of these electrodes lay in the order of tens to hundreds of micrometers. However, recent reports^[9, 10] show that the thickness of the electrodes plays an important role in their sensing characteristics such as sensitivity and response time.

Therefore, it is very interesting to manufacture NO_x -sensors using thin film (1-1000 nm thick layers) electrodes and possibly also thin film electrolytes.

For the deposition of thin films many techniques are available, such as PLD, Molecular Beam Epitaxy (MBE), Chemical Vapor Deposition (CVD) or sputtering. However, PLD has shown great versatility and ease of use over the last few decades and has been used to grow many types of oxide, nitride and metal films.

PLD is a technique that relies on the ablation of a target material by means of laser irradiation and will be fully discussed in paragraph 2.8

2.4. Ionic conductivity in stabilized zirconia

Zirconia (zirconium oxide, ZrO_2), has a monoclinic phase in its pure form at room temperature^[11]. At increased temperatures the crystal transitions successively to the tetragonal and cubic form. The phase diagram can be found below, in Figure 5. This phase diagram shows that for pure zirconia the transition from the monoclinic phase to the tetragonal phase takes place at 1100 °C and the transition from the tetragonal phase to cubic phase takes place at 2400 °C.

Substitution of a zirconium ion with another ion (of comparable ionic radius) can stabilize the tetragonal or cubic form of the crystal at room temperature, preventing the zirconia from cracking after it is cooled from the sintering temperature down to room temperature. This cracking is caused by the volume expansion that takes place at the transitions from monoclinic to cubic.

Doping with sufficient amounts of yttria (Y_2O_3) stabilizes the cubic phase. The substrates used in this research are doped with 8 mol% Y_2O_3 . The fluorite crystal structure of the cubic zirconia can be seen in Figure 4.

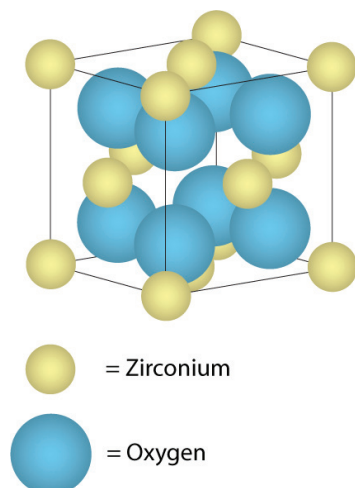


Figure 4: Zirconia crystal structure

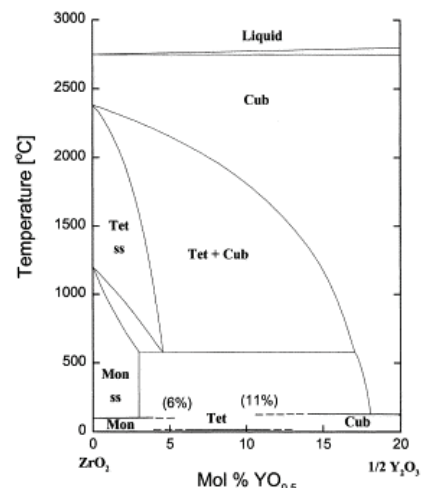


Figure 5: Phase diagram of $\text{ZrO}_2\text{-Y}_2\text{O}_3$ ^[11]

Ionic conduction in the zirconia electrolyte is induced by the substitution of the zirconium ion, which has a valency of +4, with a cation with different valency. The solid state reaction that takes place when zirconia is doped with yttria is (in Kröger-Vink notation)^[12]:



Thus, the incorporation of an oxide with a lower valency cation into zirconia will give rise to the creation of oxygen vacancies. These oxygen vacancies make a hopping mechanism possible for oxygen ions and thus greatly enhances the mobility of oxygen in the crystal. It is not true however, that an increase in the amount of vacancies (that is, an increase in the amount of dopant added) automatically increases the oxygen ion mobility in the electrolyte, since unwanted defect associates formed at high doping levels can restrict the mobility of oxygen ions and thereby decrease the ionic conductivity.

The mobility of oxygen ions in the crystal can be expressed as^[13]:

$$\sigma T = A \exp\left(\frac{-E_a}{kT}\right) \quad (2)$$

in which E_a is the process enthalpy and A is a material dependant pre-exponential factor. If this pre-exponential factor A is expanded for the case of an oxide ionic conductor in the extrinsic regime (carrier concentration is independent of temperature) we get:

$$A = C\gamma\left(\frac{Z^2e^2}{k}\right)a_0^2\nu_0 \exp\left(\frac{\Delta S_m}{k}\right) \quad (3)$$

where C is the concentration of charge carriers, γ is a geometrical factor, Ze is the charge of the carriers, a_0 is the jump distance, ν_0 is the jump attempt frequency and ΔS_m is the entropy of migration.

The concentration of carriers is considered to be determined by the amount of oxygen vacancies in the crystal lattice and can be calculated from:

$$C = N_0[V_o^{\bullet\bullet}](1 - [V_o^{\bullet\bullet}]) \quad (4)$$

where N_0 is the number of anion sites per unit volume and $[V_o^{\bullet\bullet}]$ is the concentration of oxygen vacancies expressed as a site fraction. For small values of $[V_o^{\bullet\bullet}]$ equation (4) can be reduced to:

$$C \approx N_0[V_o^{\bullet\bullet}] \quad (5)$$

Not all oxygen vacancies can act as charge carriers because the created defects (yttrium on a zirconium site, which has a net negative charge in the crystal, and the oxygen vacancies with a net positive charge in the crystal) will be attracted to each other and will form defect associates in the form of defect pairs, triplets, etc. For instance, if CaO is doped into ZrO₂ the following association reaction will take place:



These associates are immobile and are therefore detrimental to oxygen mobility in the crystal. An optimum value of the amount of dopant towards the mobility of oxygen in the crystal can be found as there will be competition between the creation of new vacancies and the creation of more associates.

At a dopant level of 8 mol% Y_2O_3 the cubic phase is stable at room temperature, as shown in Figure 5. This composition is commonly known as 8YSZ.

Consequently this material has been chosen as the substrate material on which the manufactured NO_x sensors have been built. In the rest of this report this is the material that the term YSZ will refer to.

2.5. Electromotive force

A gradient in the oxygen chemical potential across the electrolyte will give rise to an electrical potential difference between those points. This electrical potential difference is called the Electromotive Force (EMF) and an equation for this EMF will be derived in this paragraph^[14].

To probe the electrical potential difference across the electrolyte electrodes will have to be applied. A common example would be platinum electrodes, so that the galvanic cell that is constructed in that manner can be written as:



A formula for the EMF can be derived by making use of the thermodynamic equilibrium equations, which is only valid when the entire cell is in equilibrium. However, it is also possible to derive a formula for the EMF by using the Wagner theory, which assumes local chemical equilibrium. First the derivation using thermodynamic equilibria will be demonstrated, after which the Wagner theory derivation will be executed.

2.5.1. Derivation of the EMF in case of thermodynamic equilibrium

The EMF as measured by a voltage sensor would be:

$$E = \phi_{Pt}' - \phi_{Pt}'' \quad (7)$$

The electrochemical potential of the electrons in the Pt lead can be described as:

$$\tilde{\mu}_e^{Pt} = \mu_e^{Pt} - e\phi \quad (8)$$

Because the chemical potential of platinum in both the leads is equal (that of pure platinum) equation (7) can be rewritten as:

$$E = -\frac{1}{e} \left[\tilde{\mu}_e^{Pt'} - \tilde{\mu}_e^{Pt''} \right] \quad (9)$$

The equilibrium condition for transition of electrons from the platinum to the YSZ is:

$$\tilde{\mu}_e^{Pt} = \tilde{\mu}_e \quad (10)$$

$\tilde{\mu}_e$ is the chemical potential of the electrons in the YSZ electrolyte. Since this holds for both sides of the electrolyte equation (9) can be transformed into:

$$E = -\frac{1}{e} \left[\tilde{\mu}_e' - \tilde{\mu}_e'' \right] \quad (11)$$

This means that in fact the platinum leads act as probes for the chemical potential of the electrons in the YSZ.

At the interface between electrode and electrolyte there will be an equilibrium between the oxygen in the gas phase and in the bulk of the electrolyte:



When equation (12) is expressed in terms of chemical potentials this equation transforms into:

$$\mu_{O_2} + 4\tilde{\mu}_e - 2\tilde{\mu}_{O^{2-}} = 0 \quad (13)$$

If equation (13) is substituted into equation (11) the potential across the electrolyte can be expressed in terms of the chemical potential of gaseous oxygen and oxygen ions:

$$E = \frac{1}{4e} \left[\mu_{O_2}' - \mu_{O_2}'' \right] - \frac{1}{2e} \left[\tilde{\mu}_{O^{2-}}' - \tilde{\mu}_{O^{2-}}'' \right] \quad (14)$$

Since the dominant defects in the YSZ are oxygen vacancies this means that when $dn_{O^{2-}}$ oxygen ions are incorporated into the crystal there are also $dn_{\{V_O^{\bullet\bullet}\}}$ oxygen vacancies that are eliminated from the crystal, in other words $dn_{O^{2-}} = -dn_{\{V_O^{\bullet\bullet}\}}$, or expressed as partial differentials:

$$\left(\frac{\partial G}{\partial n_{O^{2-}}} \right)_{p,T} = - \left(\frac{\partial G}{\partial n_{\{V_O^{\bullet\bullet}\}}} \right)_{p,T} \Rightarrow \tilde{\mu}_{O^{2-}} = -\tilde{\mu}_{\{V_O^{\bullet\bullet}\}} \quad (15)$$

The electrochemical potential of the oxygen vacancies in YSZ can be expressed as:

$$\tilde{\mu}_{\{V_O^{\bullet\bullet}\}} = \mu_{\{V_O^{\bullet\bullet}\}} + 2e\phi = \mu_{\{V_O^{\bullet\bullet}\}}^0 + k_B T \ln \left(\frac{[V_O^{\bullet\bullet}]}{2 - [V_O^{\bullet\bullet}]} \right) + 2e\phi \quad (16)$$

This electrochemical potential is approximately constant if there is no current through the electrolyte. Due to the high concentration of oxygen vacancies in YSZ their chemical potential is nearly constant, so that the electrochemical potential as described in (16) is independent of the vacancy concentration and the electrical field for the current circumstances. Thus the second term in equation (14) is cancelled out and when the chemical potential of gaseous oxygen is written as:

$$\mu_{O_2} = \mu_{O_2}^0 + k_B T \ln p_{O_2} \quad (17)$$

the electrical potential between the two probes can be described as:

$$E \cong \frac{k_B T}{4e} \ln \left(\frac{p'_{O_2}}{p''_{O_2}} \right) \quad (18)$$

Equation (18) is a so-called Nernst equation, relating the EMF to the logarithm of the ratio of the oxygen partial pressures at probed points of the electrolyte.

2.5.2. Derivation of the EMF using Wagner theory

A second method to derive the EMF is the Wagner theory that assumes local chemical equilibria. In other words: the rate of the internal reaction with which the defects are formed is assumed to be much larger than the rate of concentration changes due to transport. Due to this assumption it is legal to assume local thermodynamic equilibrium across infinitesimal elements in the electrolyte and thus to use the associated equations.

The starting points for this derivation are the Onsager linear flux equations for all the particles or defects:

$$j_i = -L_i \nabla \tilde{\mu}_i = -\frac{D_i c_i}{k_b T} \nabla \tilde{\mu}_i \quad (19)$$

in which L_i is the transport coefficient, D_i is the self diffusion coefficient and c_i is the concentration of particle i . Possible interactions between (flows) of particles are assumed to be negligible, as is visible in equation (19) where the flux of particle i is dependant only on the electrochemical potential gradient of that particle.

An equation for the diffusion coefficient D_i is given by the modified Nernst-Einstein equation:

$$D_i = \frac{k_b T u_i}{z_i q_{el}} \quad (20)$$

When equation (20) is substituted into (19) the general flux equation becomes:

$$j_i = -\frac{\sigma_i}{z_i^2 e^2} \nabla \tilde{\mu}_i \quad (21)$$

So the specific flux equations for the transport of oxygen ions and electrons through YSZ are:

$$j_{O^{2-}} = -\frac{\sigma_{O^{2-}}}{4e^2} \nabla \tilde{\mu}_{O^{2-}} \quad (22)$$

$$j_e = -\frac{\sigma_e}{e^2} \nabla \tilde{\mu}_e \quad (23)$$

In the stationary situation these fluxes are coupled in such a way that there is no charge buildup in the electrolyte.

$$\sum_i z_i j_i = -2j_{O^{2-}} - j_e = 0 \quad (24)$$

When equations (22), (23) and (24) are combined this yields:

$$\frac{1}{2} \sigma_{O^{2-}} \cdot \nabla \tilde{\mu}_{O^{2-}} = -\sigma_e \cdot \nabla \tilde{\mu}_e \quad (25)$$

The aforementioned postulate of local chemical equilibrium can be expressed as:

$$\nabla \mu_{O_2} + 4\nabla \tilde{\mu}_e - 2\nabla \tilde{\mu}_{O^{2-}} = 0 \quad (26)$$

Using equation (25) we can eliminate $\nabla \tilde{\mu}_{O^{2-}}$ from equation (26), to find an expression for the electrochemical potential of the electrons as a function of the chemical potential of gaseous oxygen:

$$\nabla \tilde{\mu}_e = -\frac{1}{4} \frac{\sigma_{O^{2-}}}{\sigma_{O^{2-}} + \sigma_e} \nabla \mu_{O_2} = -\frac{1}{4} t_{ion} \nabla \mu_{O_2} \quad (27)$$

where t_{ion} is the fraction of the total conductivity contributed by the transport of oxygen ions.

Integrating this over the thickness of the electrolyte yields:

$$\tilde{\mu}_e' - \tilde{\mu}_e'' = -\frac{1}{4} \int_{\mu_{O_2}''}^{\mu_{O_2}' } t_{ion} \nabla \mu_{O_2} \quad (28)$$

As established in equation (11) the EMF of the YSZ electrolyte is related to the electrochemical potentials of the electrons on both sides of the electrolyte, so that the EMF follows from equation (28) as:

$$E = \frac{1}{4e} \int_{\mu_{O_2}''}^{\mu_{O_2}' } t_{ion} d\mu_{O_2} \quad (29)$$

In principle t_{ion} is a function of the chemical potential of oxygen and is dependant on the defect chemistry of the solid. To perform the integration of equation (29) it is essential to know this relationship. However, in case of a purely ionic conducting

electrolyte there is a wide range of temperatures and partial oxygen pressures in which the ionic conductivity is much higher than the electron conductivity ($\sigma_{ion} \gg \sigma_e$) and thus the transport number t_{ion} is 1. Once again expressing the chemical potential of oxygen as $\mu_{O_2} = \mu_{O_2}^0 + k_B T \ln p_{O_2}$ equation (29) is integrated into:

$$E = \frac{1}{4e} (\mu'_{O_2} - \mu''_{O_2}) = \frac{k_b T}{4e} \ln \left(\frac{p'_{O_2}}{p''_{O_2}} \right) \quad (30)$$

which is the Nernst equation as derived in the previous paragraph.

Thus, it is shown that the EMF is not only an equilibrium value, but also a dynamic value of the galvanic cell.

2.6. Non-Nernstian behavior

When a gas mixture consists of more than one oxidizable or reducible component multiple electrochemical reactions can take place at the electrode surface and so the electrode potential is determined by the rates at which the electrochemical reactions take place. This phenomenon is called mixed-potential^[15]. The concept was first introduced by Fleming^[16] to explain the non-Nernstian behavior of oxygen sensors in the gas mixture of air and fuel (an oxidizable gas).

To illustrate, the behavior of a sensor where NO and oxygen are coexistent in a gas mixture and Pt electrodes are used as both sensing and reference electrodes is shown. The reference electrode is held in a controlled reference gas environment. In this case the NO can influence the sensor in two ways.

First of all the NO may reduce the local concentration of O₂ at the surface of the electrode if this electrode works as a catalyst for the reaction (which is the case for platinum electrodes and many oxide electrodes).

An important area for the electrode is the triple phase boundary (TPB), which is the point at which electrode, electrolyte and gas phase are in contact.

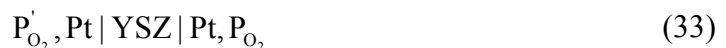
The following reaction will take place (O', NO' and NO₂' denote molecules in the vicinity of the TPB):



Since this reduces the oxygen partial pressure near the triple phase boundary the EMF across the sensor will be smaller than could be expected for the bulk oxygen concentration. The cathodic reaction for the cell in that case is:



So, in that case the electrochemical cell can be expressed as:



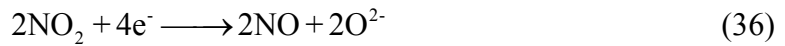
A second way in which the NO can affect the EMF measured by the cell is by reaction with the oxygen ion from the electrolyte:



In this case the electrochemical cell is expressed as:



At the sensing electrode both the reduction reaction (expression (32)) and the electrochemical oxidation reaction (expression (34)) take place and determine the potential of the sensing electrode. Similar deductions can also be made for oxidizing gases. In that case the occurring reactions are:



A more complicated situation occurs when both electrodes are exposed to the analyte gas or when the analyte gas consists of multiple components. The mixed potential is established when the electron transfer rates of the oxidation reaction of the oxygen ions and the nitrogen dioxide reduction reaction are equal^[17]. These reactions occur at different kinetic rates at the dissimilar electrodes as a result of which a potential difference establishes across the electrolyte.

2.6.1. Predicting sensor response

Quantitative consideration about this mixed potential can be made by treating the reaction rate limiting kinetics to be Butler-Volmer type^[18]. This equation describes the reaction rate (in terms of exchange current density) for an activation controlled reaction, in which the rate of reaction is determined solely by the rate of the electrochemical charge transfer process. This is an expression that is generally valid for all overpotentials (the potential difference above the equilibrium value required to produce a given current flow):

$$i = i_0 \left[\exp\left(\frac{\alpha_A n F}{RT} \eta\right) - \exp\left(-\frac{\alpha_C n F}{RT} \eta\right) \right] \quad (38)$$

in which i is the exchange current density, η is the overpotential, n is the number of electrons involved and α_C and α_A are anodic and cathodic transfer coefficients respectively.

In case of large overpotentials one of the terms in equation (38) will become very small and can be neglected, yielding so called Tafel-type behavior.

In the case of NO and O₂ this yields^[17]:

$$i_{O_2} = i_{O_2}^0 \exp\left(\frac{-4\alpha_1 F(E - E_{O_2}^0)}{RT}\right) \quad (39)$$

$$i_{NO} = i_{NO}^0 \exp\left(\frac{-4\alpha_1 F(E - E_{NO}^0)}{RT}\right) \quad (40)$$

in which E is the electrode potential, F is the Faraday constant, R is the molar gas constant, T is the temperature, E^0 is the equilibrium electrode potential, i_0 is the exchange current density and α is the transfer coefficient.

Equilibrium occurs when the reaction rates of these reactions are equal. The process has been described as a four-electron process, although this is probably an oversimplification, since the number of electrons transferred during the rate-determining step is unknown.

It is assumed that the exchange current density i will follow a power law behavior^[17] with respect to the concentration of the species, so that:

$$i_{O_2}^0 = -B_1 C_{O_2}^m \quad (41)$$

$$i_{NO}^0 = -B_2 C_{NO}^n \quad (42)$$

in which B_1, B_2, m and n are constants and C is the concentration of the species.

The mixed potential E_M is defined as the potential at which the absolute values of the exchange current densities are equal ($|i_{O_2}| = |i_{NO}|$) and thus equation (39) and (40) can be equalized and solved for $E = E_{Mix}$, yielding an expression for the electrode mixed potential:

$$E_{mix} = E_0 + m \frac{RT}{(4\alpha_1 + 2\alpha_2)F} \ln(C_{O_2}) - n \frac{RT}{(4\alpha_1 + 2\alpha_2)F} \ln(C_{NO}) \quad (43)$$

with:

$$E_0 = \frac{RT}{4\alpha_1 + 2\alpha_2 F} \ln \frac{B_1}{B_2} + \frac{2\alpha_1 E_{O_2}^0 + \alpha_2 E_{NO}^0}{2\alpha_1 + \alpha_2} \quad (44)$$

Simplified, equation (43) can be expressed as:

$$E_{mix}^* = E_0^* - nA^* \ln C_{NO} \quad (45)$$

with A^* being a constant.

This logarithmical dependence of the electromotive force on the analyte concentration is shown in many reports^[15, 19, 20].

It should however be noted that the assumption of Butler-Volmer rate-determining kinetics is not necessarily valid for all types of mixed-potential sensors. Garzon *et al.*^[17] consider the case where the reaction of the analyte is mass transport limited, while the reaction of the oxygen is obeying Butler-Volmer kinetics. This again yields a logarithmic correlation of the EMF to the concentration of analyte.

The oxygen reduction kinetics can also be expressed as the low overpotential linear approximation of the Butler-Volmer equation:

$$i_{O_2} = i_{O_2}^0 4F \frac{(E - E_{O_2}^0)}{RT} \quad (46)$$

When expression (46) is used for the oxygen reduction kinetics and diffusional mass transport limitations are assumed to be the rate limiting factor for the analyte oxidation reaction then a linear correlation can be found according to:

$$E_{mix} = E_{O_2}^0 - RT \frac{AD_{NO}C_{NO}}{2B\delta C_{O_2}^m} \quad (47)$$

In conclusion it can be stated that the form of the EMF response to changes in the analyte concentration is very dependent on the overpotential at the electrodes.

It should be noted that the effect of NO on the mixed potential is opposite in sign to that of NO₂ as NO is a reducing gas, where NO₂ is an oxidizing gas. Thus, the sensor response to a mixture of NO and NO₂ will be smaller than the response to either of the components separate.

2.7. Electrodes

In the previous paragraph the development of the EMF has been considered without specifying details for the electrodes. However, as discussed by Di Bartolomeo *et al.*^[21] the electrode material and morphology plays an important role in the sensor's response. The mixed potential model is generalized into what is called a "Differential electrode equilibria" -model, which not only takes into account the electrochemical reaction, but also the electrocatalytic activity and the adsorption-desorption behavior of the electrode. To get a better understanding of the influence of the electrode on the sensing behavior of the sensor it is useful to summarize the reactions that can take place.

At the electrode surface the following reactions can take place:

- Adsorption/desorption of the species from the gas phase (e.g., $\text{NO(g)} \rightleftharpoons \text{NO(ads)}$)
- Dissociation of the adsorbed species (e.g., $\text{O}_2(\text{ads}) \rightleftharpoons 2\text{O(ads)}$)
- Ionization of the adsorbed species (e.g., $\text{O(ads)} + 2e^- \rightleftharpoons \text{O}^{2-}(\text{ads})$)
- Diffusion of the adsorbed species to the triple phase boundary (TPB) (e.g., $\text{O}^{2-}(\text{ads, electrode}) \rightleftharpoons \text{O}^{2-}(\text{ads, TPB})$)
- Catalysis of gas phase reactions (e.g., $2\text{NO} + \text{O}_2 \rightleftharpoons \text{NO}_2$)

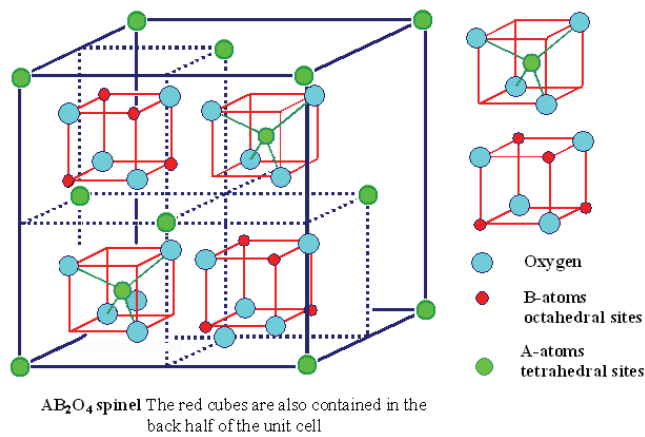
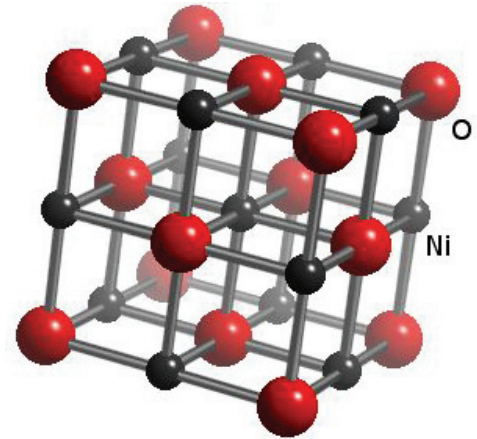
In the bulk of the electrode there can also be diffusion of oxygen ions or other species, depending on the material used for the electrode.

At the TPB there will be the exchange of oxygen ions between the electrode surface and the electrolyte (e.g., $\text{O}^{2-} + V_o^{\bullet\bullet} \rightleftharpoons \text{O}_o$).

The rate limiting step that determines the response time of the sensor could be any one of the reactions mentioned above, but could also be determined by the ionic conduction in the electrolyte.

The interplay of all these influences is a rather complex system. Zhuikov^[22] has attempted to model them mathematically, but it is still very complicated to make any predictions or recommendations for the materials choice, morphology and geometry of the electrode based on this model.

The electrode materials used, as mentioned in paragraph 2.3, are zinc ferrite (ZnFe_2O_4) and nickel(II)oxide (NiO). Zinc ferrite is a spinel type material (Figure 6), while nickel oxide has a rock salt structure (Figure 7).

Figure 6: Spinel crystal structure^[23]Figure 7: Rocksalt crystal structure^[24]

2.7.1. Metal – Metal oxide reference electrode

In steel production metal-metal oxide reference electrodes have commonly been used in determining oxygen partial pressures in melts. In this research a Ni/NiO reference electrode has been deposited.

In a metal - metal oxide reference electrode the oxidation and reduction reactions of the metal and its oxide take place:



An expression^[25] for the Gibbs free energy change of the reaction as a function of temperature is:

$$\Delta G^\circ = -RT \ln K_a = -RT \ln \frac{a_{\text{NiO}}}{a_{\text{Ni}} \sqrt{P_{\text{O}_2}}} = \frac{1}{2} RT \ln P_{\text{O}_2} \quad (49)$$

Where K_a is the equilibrium constant and a is the activity of the species. Activities of both Ni and NiO are equal to one in this case^[25] and the activity of oxygen is equal to its pressure.

The Gibbs free energy for reaction (48) can also be expressed^[26] as:

$$\Delta G_T^\circ = \frac{1}{2} (318120 - 116T \ln T) \quad (50)$$

Combining equations (49) and (50) yields:

$$RT \ln P_{\text{O}_2} = 318120 - 116T \ln T \quad (51)$$

For $T=873.15$ K (600 °C) this yields $P_{\text{O}_2}=9.95\text{E-}23$.

Thus, as long as Ni and NiO coexist in the reference electrode the oxygen chemical potential will be constant.

2.8. Pulsed Laser Deposition

As shown in paragraph 2.2 the chosen sensor geometry features two separate thin film electrodes on an electrolyte. This requires the ability to deposit and pattern thin films. Deposition is done by PLD and will be discussed in this paragraph. Patterning of the electrodes is discussed in the next paragraph.

2.8.1. Principle

The thin film deposition technique used for this research was pulsed laser deposition. The working principle for this deposition technique is the ablation of a target material using a high power laser. This ablated material then forms a plasma and expands in the direction of the substrate. On the substrate an amount of material condensates and forms a film. PLD is typically carried out in a vacuum chamber that is evacuated to remove impurities from the gas phase. Actual deposition is typically done at pressures from 10^{-3} mbar to 10^{-1} mbar for oxides and at pressures from 10^{-3} mbar to 10^{-2} mbar for metals. A background pressure is needed to reduce kinetic energy of the ablated species to prevent substrate etching by highly energetic particles and induce deposition.

In several of our depositions however, the pressure was increased up to 4 mbar, to reduce the kinetic energy of the ablated species even more, with the goal of obtaining a porous film.

The process of PLD can be described in four steps^[27]:

- Ablation of material from the target, leading to formation of a plasma
- Expansion of the plasma and possible reactions in the plasma
- Deposition of the ablated material on the substrate
- Film growth on the substrate surface

Ablation

Ablation in the first step is done by focusing a pulsed laser on the target. At an energy output of around 100 mJ per pulse (with a duration of 25 ns) at the surface of the target this transfers 4 MW of power to a small surface (in the order of several mm^2). Energy densities (fluences) of 1 to 10 J/cm^2 are sufficient to ablate most types of metals and oxides. The optimal fluence varies for different target materials. Choosing too low fluences leads to non-stoichiometric ablation whereas too high fluences lead to abundant particle emission from the target (and therefore droplet formation on the substrate).

The physical processes occurring during the irradiation of the target are beyond the scope of this report, but the result of the laser irradiation is an expanding plasma of species from the target. This plasma consists of atoms, ions, molecules, clusters of atoms and particles^[27].

Expansion

The most important impact of in the application of a background pressure is that the high energy particles are slowed down due to collisions with the background gas and will have less energy as they condensate on the surface. This affects the diffusivity of the deposited species on the surface which can be utilized to influence the morphology of the grown films^[27], as will be demonstrated in paragraph 5.2.

Deposition and film growth

The deposition and film growth on the substrate is primarily influenced by the background pressure, the substrate temperature and the substrate surface (all of which are parameters that influence the kinetic energy of the particles). Deposition takes place due to a supersaturation in the plasma, inducing condensation of material on the substrate. The composition and morphology of the surface will determine the available nucleation sites, whereas the temperature influences the surface mobility of adsorbed atoms and determines how the deposited material will crystallize.

For full oxidation of oxide films a background atmosphere of oxygen is applied.

An epitaxial relation between the grown film and the substrate, that is a film in which the crystallinity is defined by the crystal structure of the substrate, can exist for a given temperature range if lattice parameters for the film and substrate match within a certain range.

2.8.2. Setup

A schematic of the PLD setup is shown in Figure 8. In this figure the vacuum chamber is shown in which the substrate is mounted on a heater and the target is mounted on a rotating shaft. The light from the laser passes through an optical system, which masks the non-uniform part of the beam and focuses the remaining light on the target.

The used laser is a KrF excimer laser ($\lambda=248$ nm) (Lambda Physic LPX 210). The laser has a maximum pulse energy of 1000 mJ and a repetition rate between 0 and 100Hz.

Experimental procedures are summarized in 3.1.2

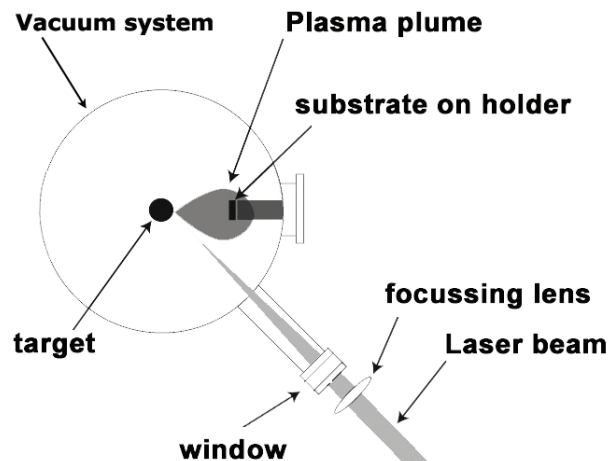


Figure 8: A typical PLD setup^[28]

2.9. Electrode patterning techniques

To create the electrodes on the electrolyte with a well defined surface area it is important to select a proper patterning technique. A patterning technique can also be useful in creating an electrode which is not a simple square, but a more complicated shape (for instance to increase the available amount of triple phase boundaries in case of a dense film).

Photolithography is a very commonly used patterning technique which can reach critical dimensions down to 45 nm, depending on the techniques used.

2.9.1. Photolithography

The process (Figure 9) consists of coating the substrate with a layer of photoresist (a photosensitive polymer) by means of spin coating. In spin coating several drops of photoresist are put on the substrate (Figure 9.1) after which the substrate is spun to create an evenly spread layer of about 1.3 micron thick (Figure 9.2).

This photoresist is illuminated through a mask to make part of the photoresist soluble (Figure 9.3).

A developer fluid is then employed to dissolve the illuminated parts (Figure 9.4).

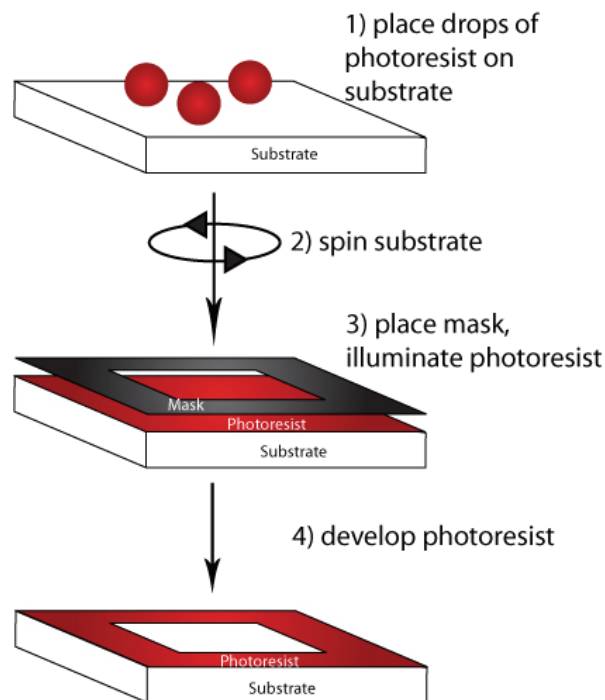


Figure 9: Photolithography

Two options exist to pattern electrodes using photolithography:

- Liftoff
- Etching

2.9.2. Liftoff

Liftoff is a process (Figure 10) in which a patterned layer of photoresist is made on a substrate by photolithography before the electrode material is deposited (Figure 10.1). After deposition (Figure 10.1) the photoresist layer is dissolved in acetone, hence removing the deposited material on top of the photoresist. Only at places where there was no photoresist, the material is left untouched (Figure 10.3). The mask used is therefore a ‘negative’ of the pattern created.

The biggest drawback of the liftoff process is that it cannot be used at elevated temperatures (above 150°C) because the photoresist would carbonize, rendering it insoluble and impossible to remove.

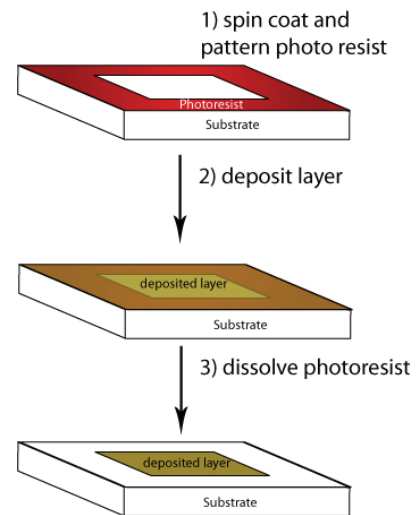


Figure 10: Liftoff procedure

2.9.3. Etching

For high temperature deposition it is therefore necessary to use the etching approach to patterning. In this case a layer of electrode material is deposited (at the chosen temperature, Figure 11.1) after which a layer of photoresist is spun onto the deposited layer. After patterning of this photoresist (Figure 11.2) (using a ‘positive’ mask) it will serve as an etch resist protecting the underlying material from the etching environment (Figure 11.3). Finally the photoresist layer is dissolved in acetone, yielding a patterned electrode (Figure 11.4).

Sputter etching was used as an etching method. In this procedure a plasma of Ar⁺ ions is created and accelerated toward the surface by an electric field.

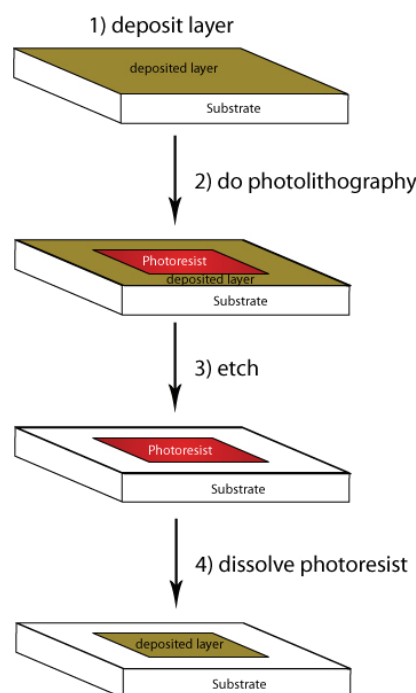


Figure 11: Etching procedure

3. Experimental

In this chapter the experimental procedures are reported.

3.1. *Electrode deposition*

Suitable electrodes have certain characteristics:

- Porous
- Correct crystalline phase
- Good adhesion to substrate

PLD is a very versatile technique, in which many parameters can be adjusted individually. Therefore it is important to find settings for fluence, pressure, target-substrate distance and deposition temperature that yield electrodes with the characteristics summed up above.

Settings are already known for NiO and Pt, but not for ZnFe₂O₄. Fluence, pressure and deposition temperature was varied for this material.

Previous work by Paul te Riele^[29], showed gas phase particle growth in Pt deposition for the pressure range from 1 mbar to 4 mbar at target-substrate distance from 40 mm to 60 mm. Deposition in this range were performed to create highly porous Pt electrode.

In the next three paragraphs an overview of the substrate treatment and deposition parameters for ZnFe₂O₄ and Pt is given.

3.1.1. Substrates

The substrates on which the depositions were performed were

- (001) Si single crystal substrates (P-type) – supplied by MESA+ cleanroom facilities
- (001) 8YSZ single crystal substrates - supplied by MTI corporation^[30], sizes were 10x10x1 mm³ or 10x10x0.5 mm³

Before deposition these substrates were cut into either 5x5 mm² or 10x5 mm² pieces using a diamond saw. The substrates were ultrasonically cleaned (Branson 2510 ultrasonic bath) for 15 minutes in acetone and ethanol, successively. After each cleaning step they were blown dry with nitrogen.

3.1.2. Deposition parameters ZnFe₂O₄ electrodes

For every different target material an optimum fluence (energy density per pulse) exists, which needs to be determined before any useful depositions can be done.

An optimal fluences for the deposition of ZnFe₂O₄ was unknown. Therefore it was determined by depositing ZnFe₂O₄ at different fluences and analyzing the deposited

films and the target surfaces after deposition with SEM. Table 4 shows the deposition parameters for the fluence determination of ZnFe_2O_4 targets.

Once the fluence is known it is of great use to measure the deposition rate of the target material for a variety of pressures. Deposition rates are measured by using the liftoff technique as described below in paragraph 2.9 to create features on a substrate. A high density of features is desired as this makes it easier to find one with Atomic Force Microscopy (AFM, see paragraph 3.3.1). From the height of the features a deposition rate can be calculated. The deposition rate of ZnFe_2O_4 was determined for oxygen pressures of 0.05, 0.1 and 0.2 mbar using the deposition parameters shown in Table 5. In Table 6 the deposition parameters are recorded for the deposition of ZnFe_2O_4 layers at different substrate temperatures.

Table 4: Deposition parameters for the fluence determination of ZnFe_2O_4 targets

Constant		
Substrate	Si	
Target	ZnFe_2O_4	
P_{O_2}	0,1	[mbar]
O_2 flow	15	[ml/min]
T	20	[°C]
$d_{\text{target-substrate}}$	48	[mm]
Frequency	5	[Hz]
#pulses	3000	
spot size	2,6	[mm ²]
Variations		
Sample	Fluence (J/cm ²)	
WB03	2	
WB04	3	
WB05	4	

Table 5: Deposition parameters for the determination of deposition rate for ZnFe_2O_4

Constant		
Substrate	YSZ	
Target	ZnFe_2O_4	
Fluence	3	[J/cm ²]
O_2 flow	15	[ml/min]
T	20	[°C]
$d_{\text{target-substrate}}$	48	[mm]
Frequency	5	[Hz]
#pulses	4500	
spot size	2,6	[mm ²]
Variations		
Sample	P_{O_2} (mbar)	
WB06	0.1	
WB07	0.05	
WB08	0.2	

Table 6: Deposition parameters for ZnFe_2O_4 at different temperatures

Constant		
Substrate	YSZ	
Target	ZnFe_2O_4	
P_{O_2}	0,1	[mbar]
O_2 flow	15	[ml/min]
$d_{\text{target-substrate}}$	48	[mm]
Frequency	5	[Hz]
#pulses	18000	
Spot size	1,95	[mm ²]
Fluence	3	[J/cm ²]
Variations		
Sample	T (°C)	
WB35	20	
WB36	300	
WB38	600	
WB39	20	

3.1.3. Deposition parameters Pt electrodes

The influence of target-substrate distance and gas pressure on the morphology of the deposited layers was investigated for platinum. The parameters for these depositions are shown in Table 7.

Table 7: Deposition parameters for Pt at different target-substrate distances and varying pressures

Constant			
Substrate	Si		
Target	Pt		
Temperature	20	[°C]	
Frequency	5	[Hz]	
Spot size	1,95	[mm ²]	
Fluence	5	[J/cm ²]	
Variations			
Sample	P _{Ar} (mbar)	d _{target-substrate} (mm)	#pulses
WB13	0,4	48	27000
WB14	0,8	48	27000
WB15	0,97	48	36000
WB16	0,97	40	36000
WB17	0,97	58	36000
WB20	2	48	36000
WB21	2	40	36000
WB22	2	58	36000
WB18	4	48	36000
WB19	4	40	36000

3.1.4. Gold sputtering

To assure a stable reference electrode, the Ni/NiO binary mixture must be properly sealed from its environment. The oxygen impermeable seal must prevent oxygen from flowing out or into the system, ensuring a long lifetime of the electrode.

Therefore the Ni/NiO electrodes were capped with a gold layer that is applied using the AC sputtering technique. A Perkin-Elmer Sputtering system model 2400 equipped with a gold target was operated at 150W and 700V bias voltage, yielding a deposition rate of 25 nm/min. The substrate was attached to the substrate holder by using double-sided tape while the part of the substrate that was not to be covered with gold was either covered with photoresist (for O₂-sensor 1) or with a piece of Teflon tape. Sputtering took place for 20 minutes to produce a gold layer of 500 nm thick.

3.1.5. Manufactured sensors

The electrodes used on the sensors were deposited using the parameters mentioned in Table 8. The row for Ni/NiO describes the deposition parameters for the constant potential reference electrode as described in paragraph 2.7.1.

Table 8: Deposition parameters for the electrode materials

	Pt	Ni/NiO (RE)	NiO	ZnFe ₂ O ₄	
Gas	Ar	O ₂	O ₂	O ₂	
P _{gas}	0,02	0,015	0,05	0,1	[mbar]
Gas flow	6	4	15	15	[ml/min]
Frequency	10	3	5	5	[Hz]
Spotsize	1,95	1,99	1,99	2,5	[mm ²]
Fluence	5	5	5	3	[J/cm ²]
d _{target-substrate}	48	45	45	48	[mm]
#pulses	16000	5760	9000	18000	
Thickness	304		250	287	[nm]

Several electrodes were manufactured based on the planar design shown in Figure 3. For all the sensors a 8YSZ substrate of 10x5x1 mm was used. The details for the sensors are shown in Table 9

Table 9: Details for the manufactured sensors

Sensor	Electrode 1	Electrode 2
O ₂ sensor 1	Pt	Ni/NiO
O ₂ sensor 2	Pt	Ni/NiO
NO _x sensor 1	ZnFe ₂ O ₄	Pt
NO _x sensor 2	NiO	Pt
NO _x sensor 3	NiO	Ni/NiO
NO _x sensor 4	ZnFe ₂ O ₄	Ni/NiO

3.2. Patterning of the electrodes

3.2.1. Photolithography

Photolithography was used to pattern the electrodes on the substrate. The procedure for the photolithography was as follows:

A few drops of Shipley 813 photoresist were spin coated onto the substrates at 5000 rpm, for 30 seconds. The substrate was then baked at 100 °C for 10 minutes to harden the photoresist. Development of the resist was done on a Karl-Süss wafer stepper.

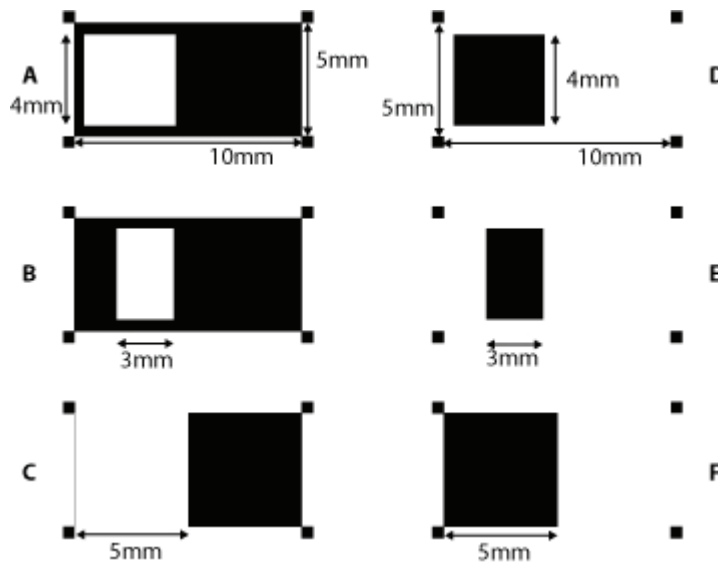


Figure 12: Masks used in photolithography. A to C are lift-off masks, D to F are etch masks. A and D: open electrode. B and E: covered Ni/NiO electrode. C and F: Au capping layer.

The masks used are shown in Figure 12. The Ni/NiO reference electrode is made smaller than the electrodes that are exposed to a gas to ensure complete coverage with gold. Masks A and D from Figure 12 were used to pattern the electrodes that are to be exposed to gas. The Ni/NiO electrode was made using masks B and E and then masks C and F were used to deposit a gold capping layer, as described in paragraph 3.1.4. Development of the photoresist was done in Shipley 531 developer for 60 seconds, after which the samples were rinsed in two baths of demi-water for 30 seconds each. Finally the sample was blown dry with nitrogen.

Removal of the photoresist layer used in lift-off was done by submerging the sample in acetone for approximately 15 minutes or until all the material was removed (judging by eye). If the deposited layer on the photoresist did not release from the substrate ultrasonic treatment was applied for a few seconds.

3.2.2. Etching

Layers deposited at temperatures above 100 °C cannot be patterned by a lift-off technique and have to be patterned using physical etching.

The etching was done in a Perkin-Elmer Sputtering system model 2400, using argon RF plasma sputter etching. Electrode size in the sputter system is 314 cm^2 .

The etch rate of ZnFe_2O_4 was determined by depositing a layer of ZnFe_2O_4 on a $10 \times 5 \times 1 \text{ mm}^3$ YSZ substrate, using the deposition parameters as reported in Table 8, but at a substrate temperature of $600 \text{ }^\circ\text{C}$ instead of $20 \text{ }^\circ\text{C}$. Subsequently a photoresist layer was applied and patterned with a mask that had many step features. This sample was then etched at 150W for 1 minute after which the photoresist was removed and the vertical height of the etched features was determined using AFM (see paragraph 5.1.3).

A similar deposition of ZnFe_2O_4 was done after which the sample was patterned using mask D from Figure 12. This sample was etched at 150W for a total of 45 minutes subsequently, after which the photoresist was removed.

3.3. *Electrode analysis*

For the analysis of the deposited electrodes several techniques were used to get information about layer thickness, morphology and crystal structure. These techniques are described in this paragraph.

3.3.1. AFM

Atomic Force Microscopy (AFM) was used to determine the morphology of some of the deposited layers. All scans were done using a Nanoscope IV microscope in contact mode. Images were processed using the Nanoscope software (version 6.13r1)

3.3.2. SEM

To gain insight in the structure of the deposited layers Scanning Electron Microscopy was employed, using the secondary electron detector of a Jeol JSM 5610 SEM.

To prevent charge-up of the sample surface the samples were coated with a thin layer of gold, if needed. This gold was deposited by the same sputtering procedure as described in 3.1.4, but with a power of 150W for 30 seconds, yielding a 12.5 nm thick layer of gold.

When this Jeol SEM was unable to resolve features at the desired magnifications a LEO 1550 FEG SEM was used, operated by Mark Smithers.

3.3.3. XRD

To investigate the crystal structure of a layer X-Ray Diffraction was used. Both an Enraf Nonius Diffractis 586 and a Philips X'pert MPD diffractometer were used. The performed scans were ω - 2θ scans along the $\langle 001 \rangle$ direction, with 2θ ranging from 6° to 120° on the Enraf Nonius diffractometer and from 8° to 70° on the Phillips diffractometer. Both machines use Cu K_α radiation of 1.54 \AA .

3.4. Gas flow measurements

After the sensors are made they need to be characterized in terms of their response to a change in the gas environment. For that purpose a gas flow system has been developed and used to characterize the sensors.

3.4.1. Gas flow setup

To examine the response of the sensor to different concentrations of gases it is necessary to have a setup in which the electrodes are exposed to a controlled gas flow while the sensor is heated to a certain temperature. The time-resolved response of the sensor (in terms of the electrical potential between the electrodes) must be measured and recorded.

The final design of the gas flow setup is shown in Figure 13.

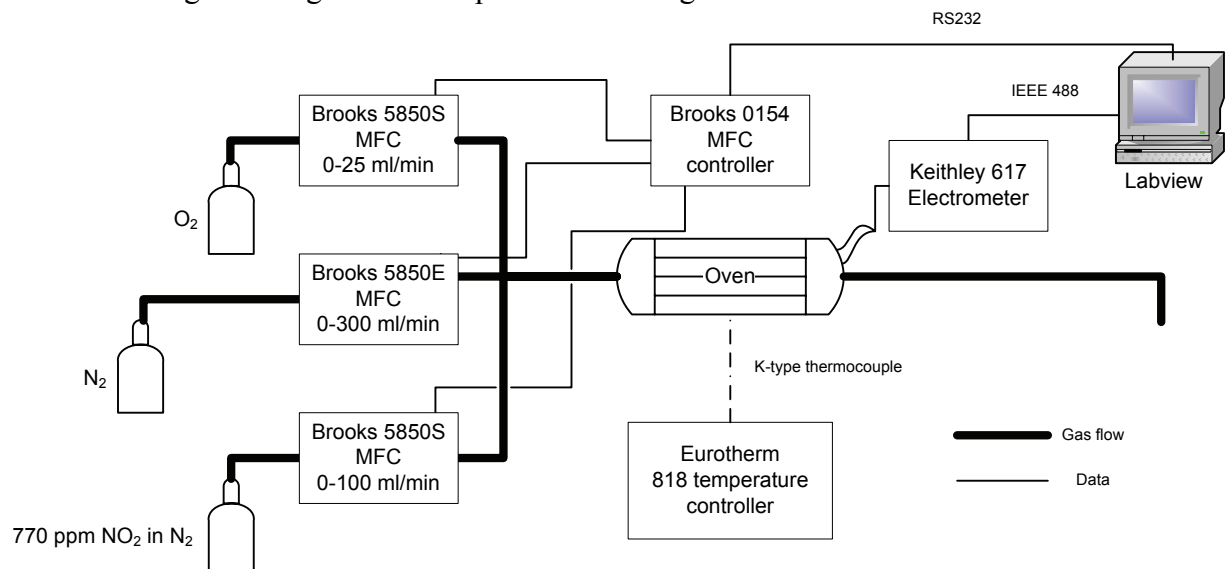


Figure 13: Gas flow setup

This design can compose a gas flow based on the three available gases (O₂, N₂, 770ppm NO₂ in N₂) with a possibility of adding a fourth gas if needed. A computer running a Labview program controls the gas flow by means of the Brooks 0154 controller, which can control up to 4 Mass Flow Controllers (MFCs) and reads out the sensor potential as measured by the Keithley 617 electrometer ($10^{12} \Omega$ input impedance). The sample can be heated by means of a tube oven controlled by a Eurotherm 818 temperature controller, equipped with a k-type (chromel/alumel) thermocouple (stability of the oven is 0.1 °C). To minimize heat losses and temperature fluctuations the oven is covered with an insulating cover.

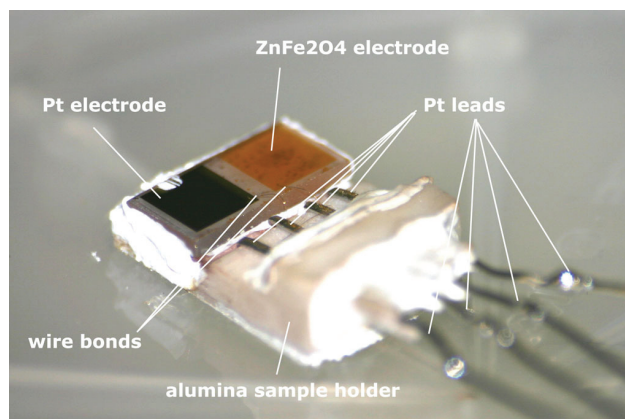


Figure 14: NO_x sensor 1 on sample holder

The samples are glued on a custom made alumina sample holder (see Figure 14) by using ceramic paste. The electrodes are wire bonded (using an Uthe Power Logicon 10G wire bonder) to the platinum leads on the sample holder using gold wire and the platinum leads are then extended through an alumina tube. Gold wires are used for wire bonding because of their compatibility with the used temperatures and their inertness.

The sample holder and alumina tube are inserted into a quartz tube which is mounted in the oven. Connections to the quartz tube are made using Swagelok couplings.

The quartz tube that is used inside the oven has an inner diameter of 12 mm to be able to accommodate the sample holder. To reduce the gas volume (and thus residence time of the gas) a smaller quartz tube has been melted inside the larger quartz tube on one side, locally reducing the inner diameter to 6 mm, as shown in Figure 15.

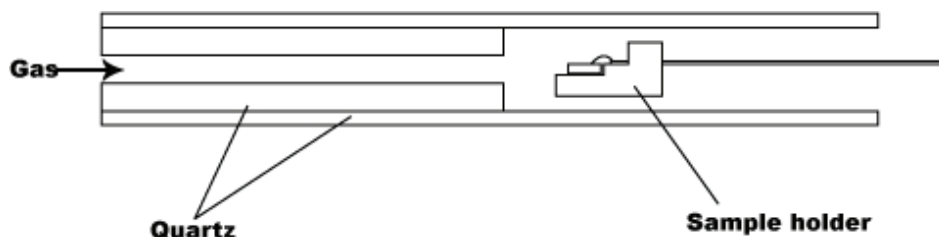


Figure 15: Quartz tube

The gas lines between the flow controllers and the sensor have been kept as short as possible, again to reduce the volume of gas and thus the time it takes before a change in flow propagates to the sensor.

The concentrations of NO₂ that are of interest for the characterization of the sensors lie between 0 and 500 ppm (in moles). Common flow rates that are used for sensor characterizations are 100 to 200 ml/minute. A premixed gas of 770ppm NO₂ in N₂ is used because of safety issues (NO₂ is corrosive and very toxic) and for accurate adjustment of the NO₂ concentration in the gas flow.

3.4.2. Characterization of gas flow setup response time

It is expected that the sensors have a given response time (in the range of several seconds to several minutes) before the full potential belonging to a certain gas

environment is reached after gas concentrations are changed. However, there will also be a finite amount of time before the gas concentrations at the sensor change after a change is applied in the control software. Thus, the signal response of the sensor will be influenced both by the sensor itself and the gas flow setup. It is therefore necessary to determine the response time of the gas flow setup.

This has been done by applying a flow of O₂ and then switching to a flow of N₂ at the same flow rate and vice versa. The concentrations of O₂ and N₂ were then measured as a function of time, using a Pfeiffer Vacuum Omnistar mass-spectrometer. Measurements were taken at the start of the quartz tube and at the end. Flow rates that were used were 50, 100, 150 and 200 ml/min.

3.4.3. Sensor response characterization

The sensitivity of the sensor to NO₂ as well as the response time was determined by supplying a gas flow of 150 ml/min and increasing the NO₂ concentration from 0 ppm to 500 ppm and back to 0 ppm in steps of 100 ppm, with a step time of 5 minutes. O₂ concentration was kept constant at 5% and the flow was kept at 150 ml/min by adjusting the N₂ flow appropriately.

To investigate the sensor's sensitivity to O₂ concentrations a flow of 150 ml/min was applied, composed of 220 ppm NO₂, N₂ and varying concentrations of O₂. The O₂ concentration was varied from 1% to 13%, in steps of 2%, with a step time of 5 minutes.

In all cases the Pt electrode was connected to the negative lead of the electrometer.

4. Gas flow setup control software design

For a simple control and read-out of the gas flow setup a Labview program was developed. In this chapter the design of that program will be discussed.

4.1. Requirements

The program should be able to perform the following tasks:

- Allow the creation of measurement programs, consisting of a series of timed steps of certain gas concentrations
- Adjust gas flow rates
- Record gas flow rates
- Record voltage measured by electrometer
- Apply a voltage for use in potentiometric titrations
- Plot the recorded voltages as a function of time
- Store the recorded gas flow rates and voltages as a function of time in an easily usable format

The design of the software is made by using data flow diagrams, in which the interfaces and process are depicted as cubes and circles, connected by arrows representing data and event flow. A legend is given in Figure 16.

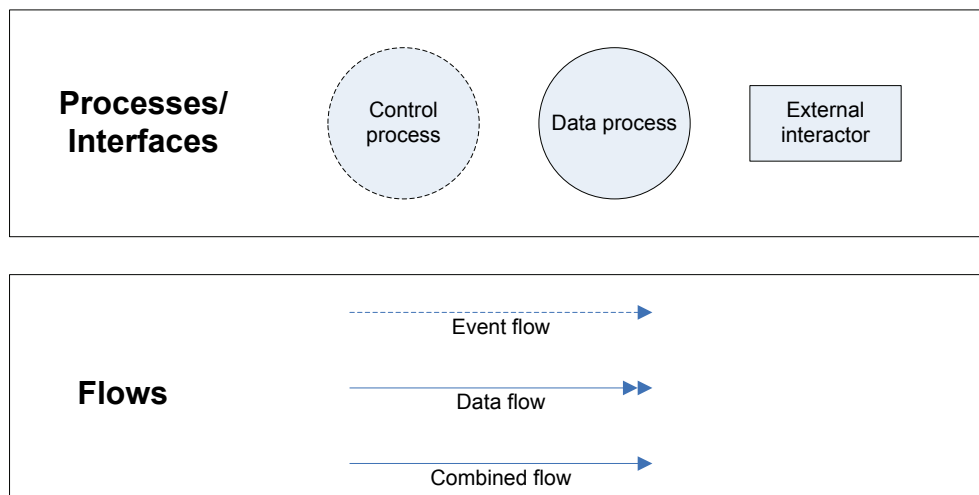


Figure 16: Legends for symbols in DFDs

Possible flows in this type of diagram are :

- Event flow - triggers an interface or process into an action but contains no data.
- Data flow - contains only data, but is not a trigger for a process or interface.
- Combined flow - contains both data and an event.

Processes and interfaces can be categorized as:

- Control process – controls other processes, has only event flows as inputs and outputs
- Data process – processes incoming data, can have all types of flows as inputs and outputs
- External interactor – Interface external to the software, can have all types of flows as inputs and outputs

4.2. Environmental model

To get an overview of the external interfaces with which the program has to communicate an environmental model was composed according to the nomenclature mentioned above. This environmental model is shown in Figure 17.

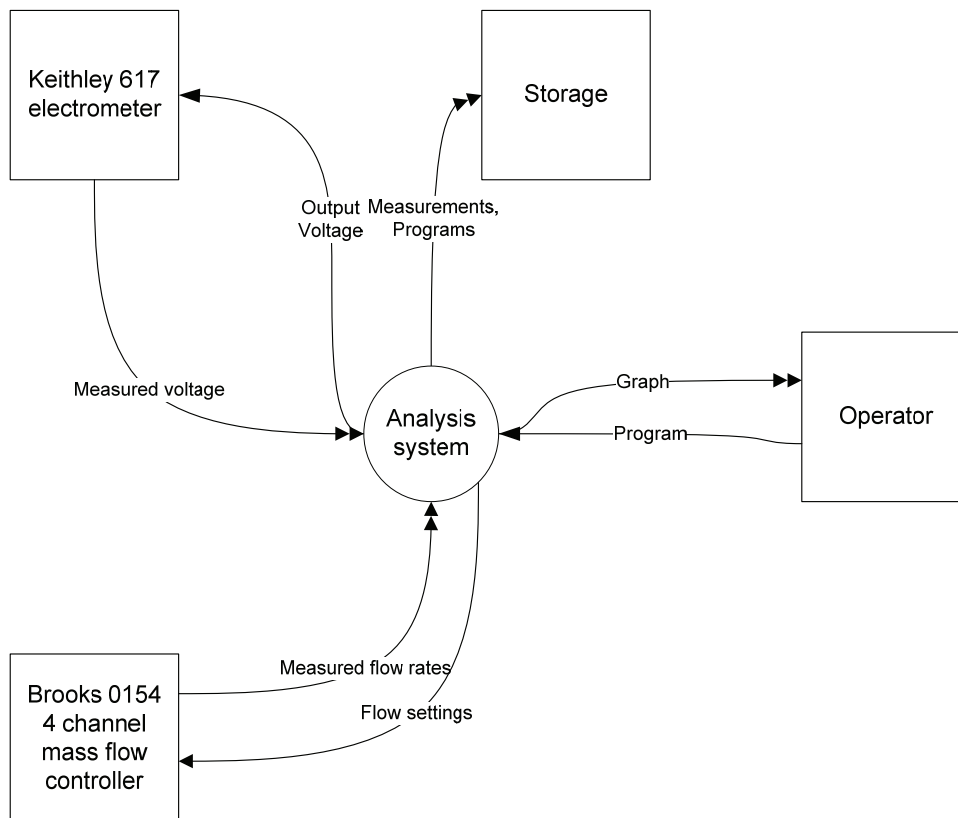


Figure 17: Environmental model for the gas flow setup control software

4.3. Data flow diagram for processes

In the environmental model the interactions of the program with the environment are summarized. Further specification of the system is done in a data flow diagram (DFD), which is shown in Figure 18 for the entire program. The lines follow the same conventions as described above.

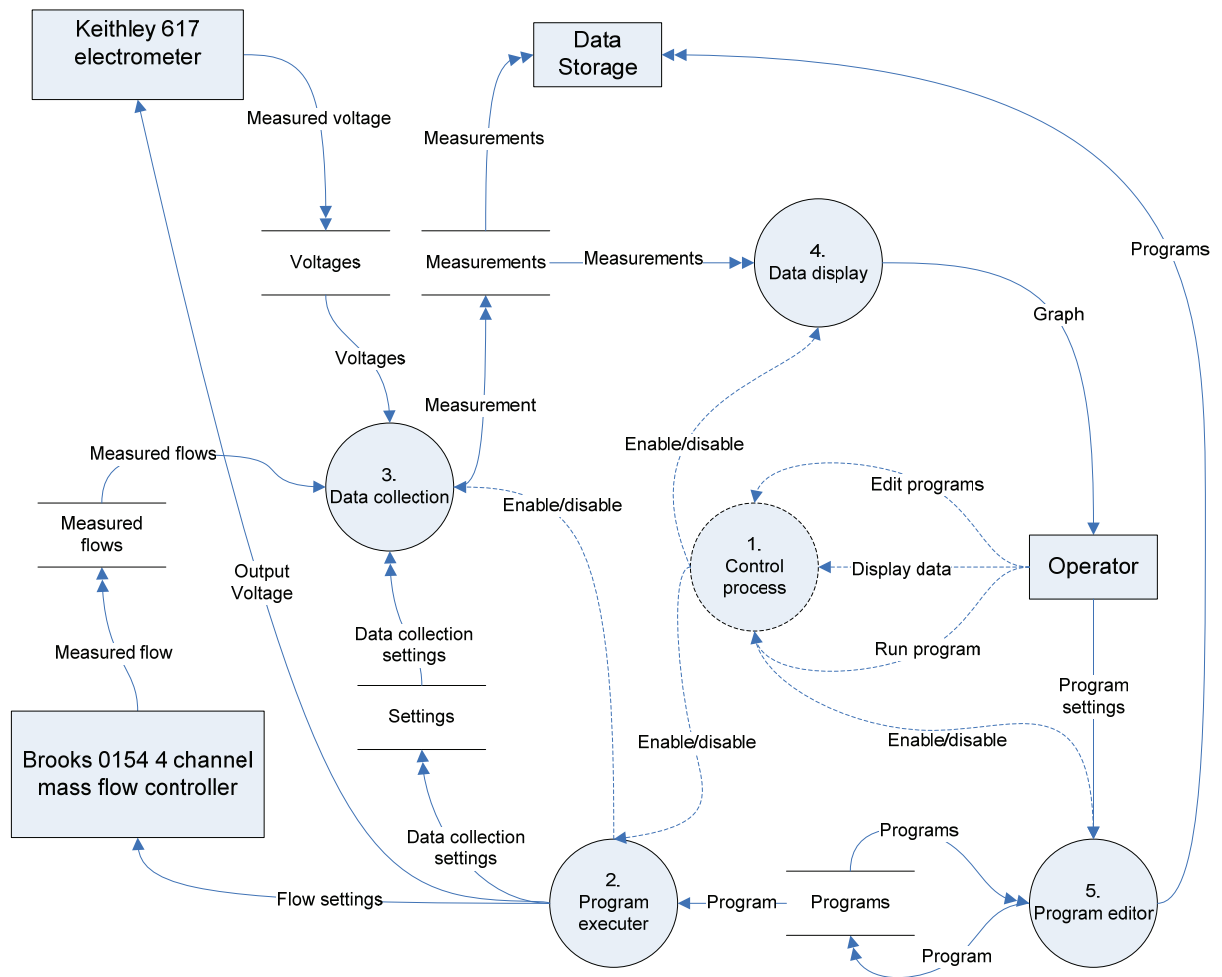


Figure 18: Data flow diagram for the gas flow setup control software

The control process takes the commands of the operator as input and enables or disables data processes accordingly.

The program executor process is responsible for setting the correct flows as indicated by a program. A program consists of several steps of a certain duration during which a concentration of each of the gases is set. A detailed DFD for the program executor process is shown in Figure 19.

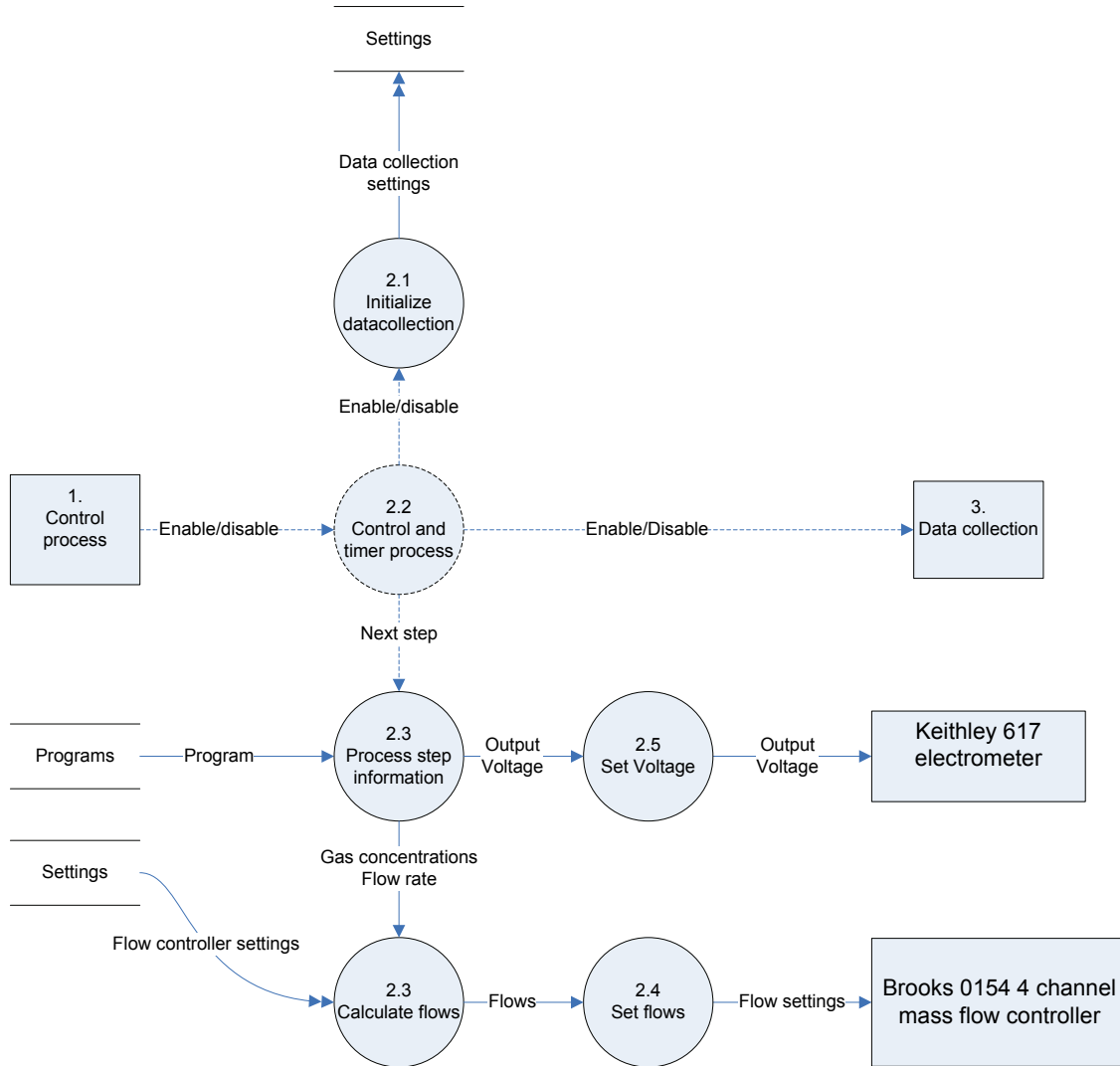


Figure 19: DFD for the program executor process

Collecting the data is done by the data collection process by polling the electrometer and Brooks 0154 every second. This data is then immediately written to a file to prevent data loss in case of power failure or system crash.

The sensor response is shown to the operator as a graph by the data display process.

Finally, the program editor process makes it possible to create and edit programs. These programs are stored in a file on disk so that they can be reused.

5. Results

In this chapter the results of the deposition of the various electrode layers will be discussed, as well as the analysis of the gas flow setup that was built. Also the fabrication and characterization of the sensors is discussed.

5.1. ZnFe₂O₄ electrodes

5.1.1. Fluence determination

The optimal fluence for deposition of ZnFe₂O₄ thin films has been determined by SEM analysis of the target surface and of the surface of the deposited thin film after depositions at various fluences.

An overview of the target surfaces after deposition at varying fluences was made earlier by Frank Vroegindeweij and is shown in Figure 20.

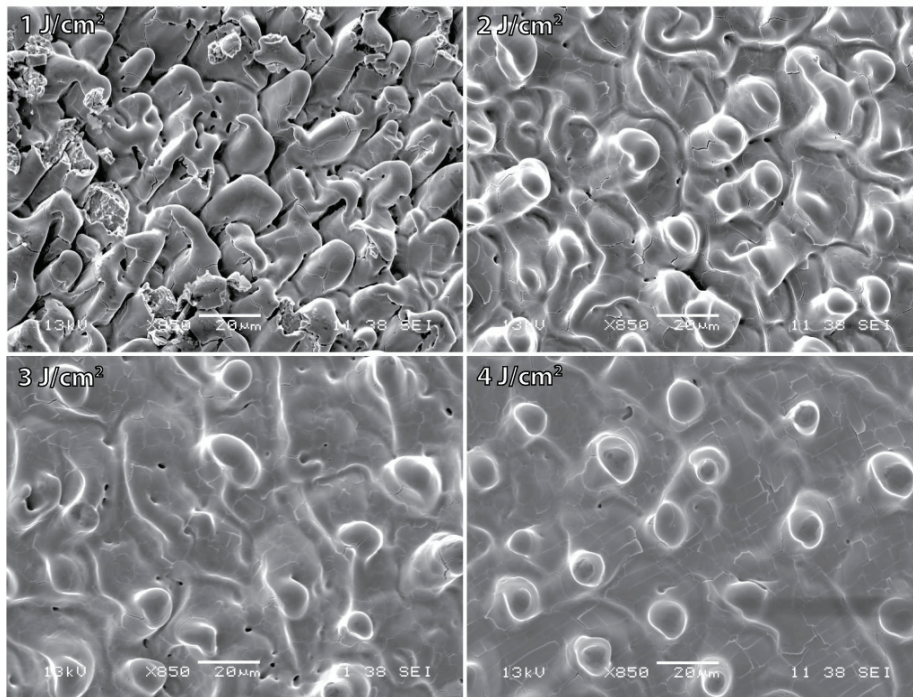


Figure 20: The surface of a ZnFe₂O₄ target after 200 pulses on the same spot (no rotation)

Chrissey and Hubler^[27] describe that laser irradiation at PLD fluence levels can cause the formation of cones on the target. These cones can be seen to appear at fluence levels of 2 J/cm² for ZnFe₂O₄, judging by Figure 20. At 3 J/cm² and 4 J/cm² the cones appear to be more uniformly shaped than at 2 J/cm². Too low fluences might lead to incongruent evaporation when certain elements are evaporated at non-stoichiometric amounts. However, too high fluences might aggravate the problem of large, unwanted particulates that are ejected from the target surface and will deposit on the sample surface. Therefore the sample surface for each of the depositions was analyzed to estimate the amount of particulates on the surface. The results are shown in Figure 21.

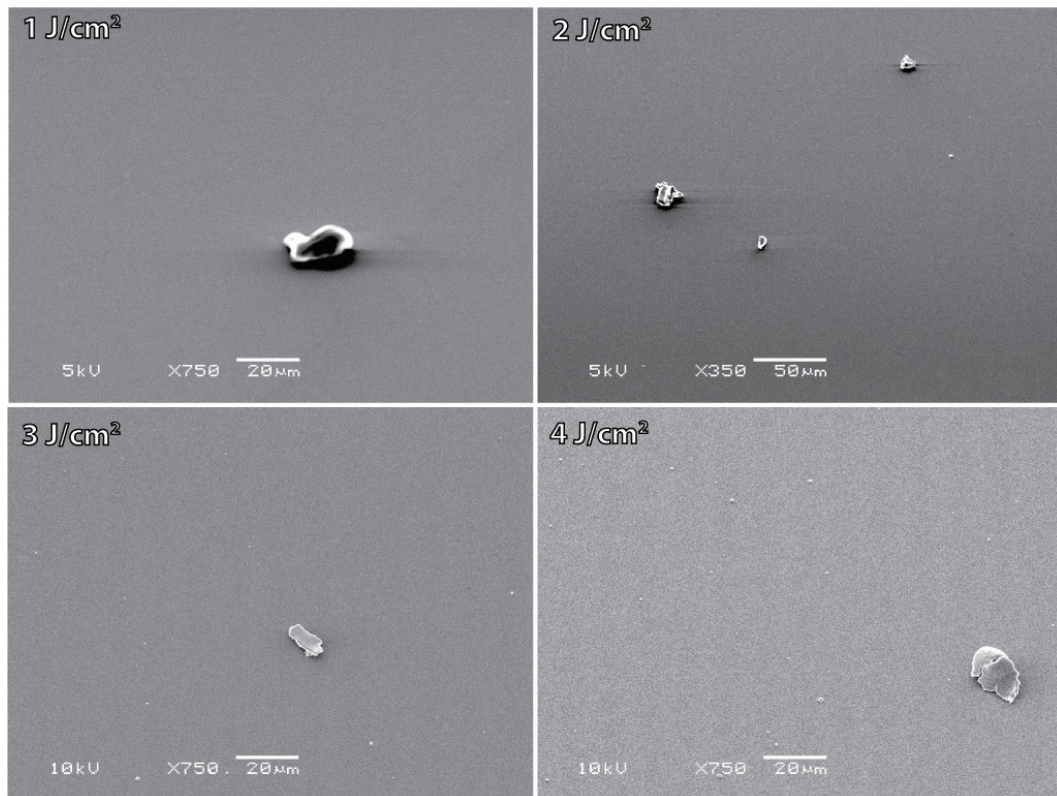


Figure 21: SEM image of sample surfaces after 3000 pulses at various fluences

The small dots seen in Figure 21 are particulates and the larger objects are most likely dust particles or parts of the layer that have been scraped off. This figure shows that for fluences of 2 J/cm^2 and above there is deposition of particulates on the sample. A fluence of 3 J/cm^2 has been chosen as the most optimal compromise between uniform evaporation (as indicated by cone formation) and acceptable amounts of particulates on the sample.

5.1.2. Deposition rate determination

A layer of ZnFe_2O_4 (deposition parameters as found in Table 5) was patterned by liftoff, as described in 2.9. A deposited feature as imaged with AFM is shown in Figure 22. The average height of this feature was determined. Three features (selected at random) were imaged per substrate. An overview of the deposition rate as a function of oxygen pressure is shown in Figure 23. An average deposition rate of 0.17 \AA/pulse was determined in the pressure range of 0.04 to 0.20 mbar O_2 . It is clear that the deposition rate is not dependant on gas pressure in this range of oxygen pressures.

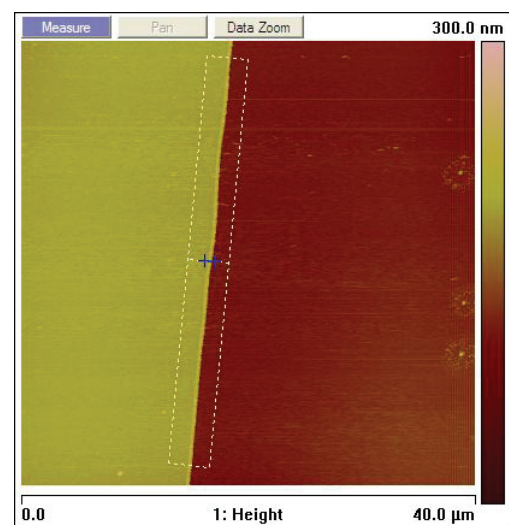


Figure 22: AFM image of feature on sample WB07 after 4500 pulses

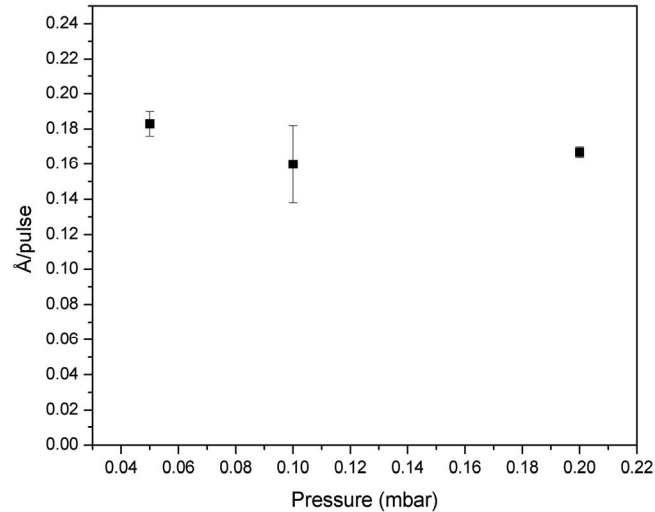


Figure 23: Deposition rate for ZnFe₂O₄ as a function of pressure

5.1.3. Etch rate determination

The etch rate of ZnFe₂O₄ was determined as described in 3.2.2. Etched features were imaged with AFM (as shown in Figure 24). Features at three locations on the sample were imaged. The etch rate was determined to be 14.2 ± 1.2 nm/min at 150W (electrode size is 314 cm², yielding an power density of 0.47W/cm²).

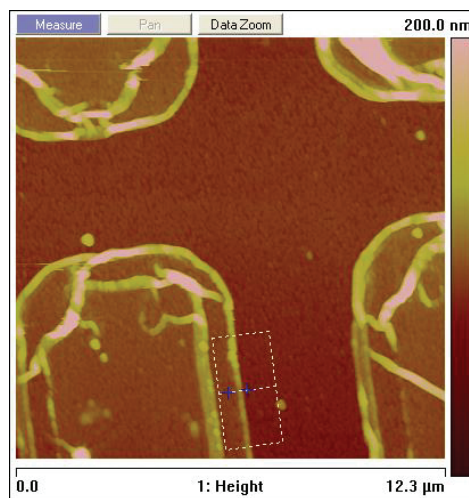


Figure 24: AFM image of feature used for etch rate determination

5.1.4. Influence of deposition temperature on crystallinity and microstructure of ZnFe_2O_4 thin films

Thin films of ZnFe_2O_4 were deposited on 8YSZ substrates (deposition parameters as mentioned in Table 6) at 20, 300 and 600 °C to determine the influence of substrate temperature on film morphology and crystal structure. The as-deposited films were imaged by AFM (Figure 25) from which the RMS roughness and the average grain size were determined (Table 10).

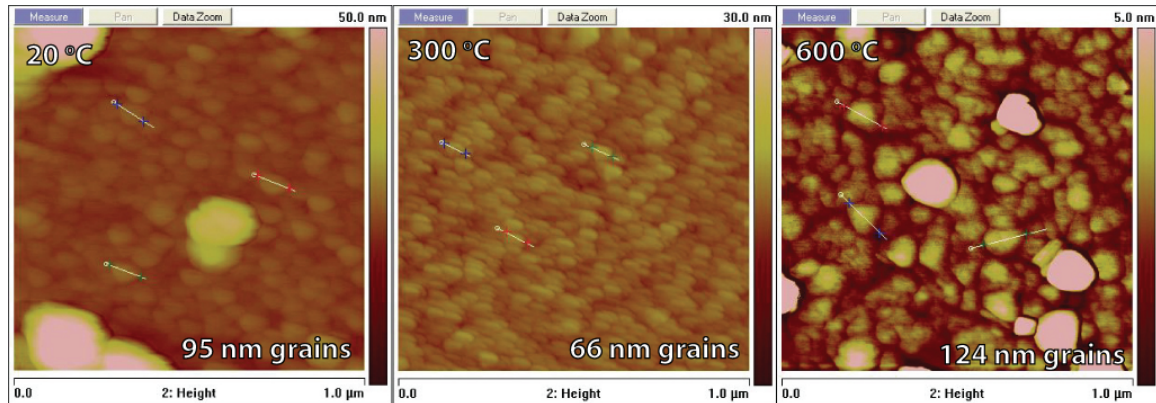


Figure 25: AFM images of ZnFe_2O_4 films deposited at 20, 300 and 600 °C

Table 10: roughness and grain size for ZnFe_2O_4 films deposited at 20, 300 and 600 °C

Sample	Deposition Temperature (°C)	RMS roughness (nm)	Average Grain size (nm)
WB39	20	4,81	95
WB36	300	1,34	66
WB38	600	0,99	124

The deposited layers were analyzed using XRD to get information about the crystal structure. ω -2 θ scans were performed from $2\theta=6^\circ$ to $2\theta=120^\circ$ for all the deposited films. The XRD spectra (displayed with a vertical shift for visual clarity) are plotted in Figure 26.

For all three films the YSZ(002) and YSZ(004) substrate peaks are visible.

The films deposited at 300 °C and 600 °C show cubic ZnFe_2O_4 {111} reflections and several other peaks (unassigned in Figure 26) that have been assigned as higher order reflection of the 8YSZ substrate. These peaks will not be visible on the Philips diffractometer because its receiving optics are equipped with a graphite monochromator, eliminating higher order reflections.

The ZnFe_2O_4 {111} reflections are stronger in the sample deposited at 600 °C than in the one deposited at 300 °C, indicating an higher amount of ZnFe_2O_4 (111) phase at the higher temperature.

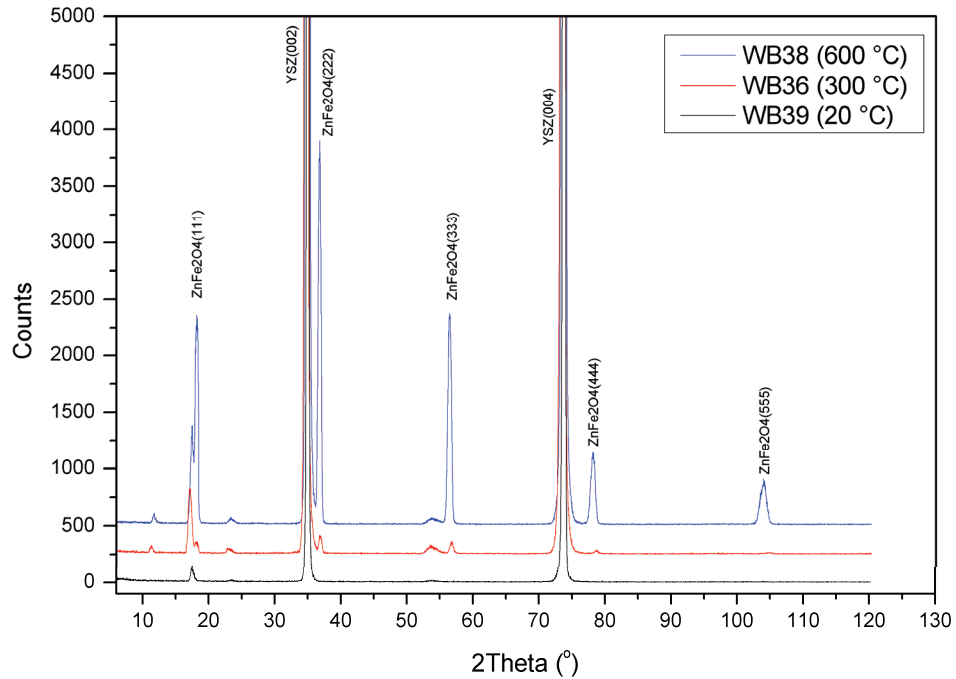


Figure 26: XRD spectra for ZnFe₂O₄ films deposited at 20 °C, 300 °C and 600 °C

The substrates were broken in half, coated with 12.5 nm of gold (as described in 3.1.4) and SEM cross section images were made to determine the structure of the layer. These images are shown in Figure 27.

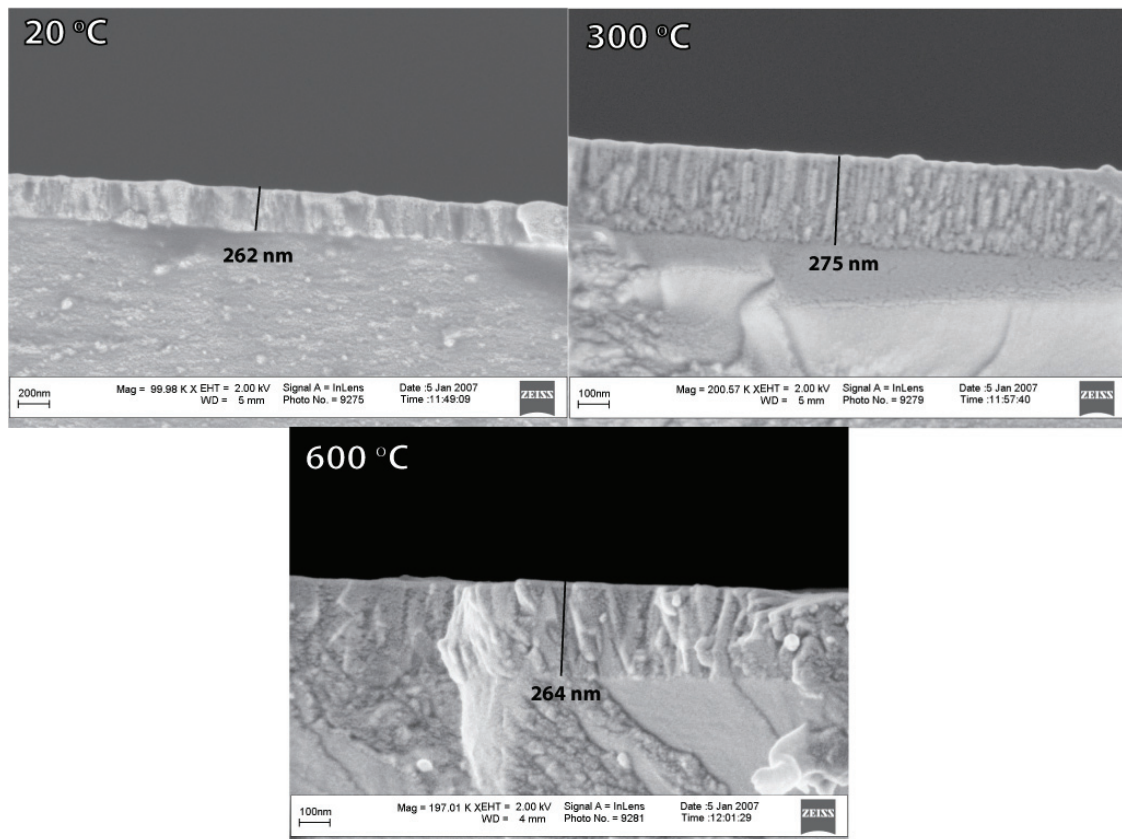


Figure 27: SEM cross section images of as-deposited ZnFe₂O₄

All three films appear to be dense (as observed by SEM, oxygen permeability is unknown) and (microscopically) smooth at an approximate thickness of 270 nm. The film deposited at 20 °C has very small grain structures that are not very well visible on the SEM image. The film deposited at 300 °C has a structure featuring small fibrous grains. A more rough plane of fracture is observed for the film deposited at 600 °C, which seems to have some grains protruding from that plane.

5.1.5. Influence of annealing temperature on crystallinity and microstructure of ZnFe₂O₄ thin films

To investigate the influence of annealing temperature on the crystallinity and microstructure of ZnFe₂O₄ thin films the sample deposited at 20 °C (sample WB39) was annealed for 10 hrs under atmospheric conditions at 300 °C, 600 °C, 900 °C and 1200 °C subsequently. XRD spectra were recorded after each annealing step while AFM and SEM images were taken after annealing at 1200 °C.

The XRD spectra are shown in Figure 28. All scans are made on the Enraf-Nonius diffractometer, unless indicated otherwise. No new peaks have appeared after annealing up to 900 °C, which means that there are no new phases formed that have any reflections in the plane scanned. The film annealed at 1200 °C shows several new peaks, that have been attributed to Fe₂O₃ (PDF reference code 01-071-6338), Fe₃O₄ (PDF reference code 01-084-0307). This composition of phases suggest a Zn deficiency has arisen during annealing at 1200 °C, assuming stoichiometric deposition of the ZnFe₂O₄ layer during PLD.

A change of the surface after annealing at 1200 °C could be noticed by the naked eye: the surface was more dull and a different shade of brown than before annealing. The microstructure of the film was analyzed by AFM and SEM. The SEM image (Figure 30) shows that the continuous film of ZnFe₂O₄ has been transformed into a number of islands, which range from 1 to 10 μm in length and are non-uniformly shaped. Their height ranges from 150nm to 1μm, judging from the AFM image.

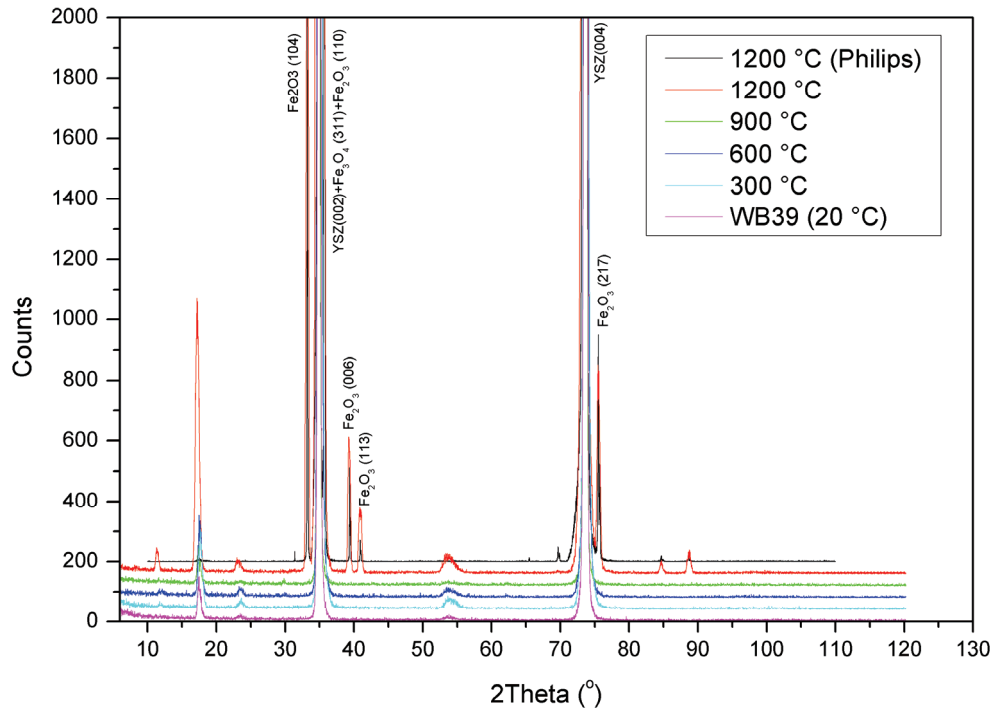


Figure 28: XRD spectra of sample WB39, as deposited (20 °C) and after annealing for 10 hrs at 300 °C, 600 °C, 900 °C and 1200 °C

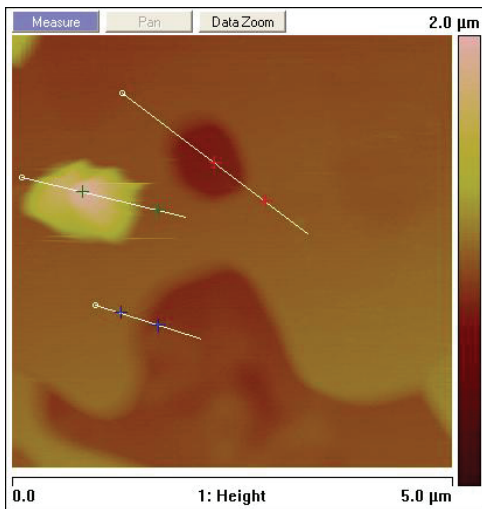


Figure 29: AFM image of sample WB39, annealed at 1200 °C for 10 hrs

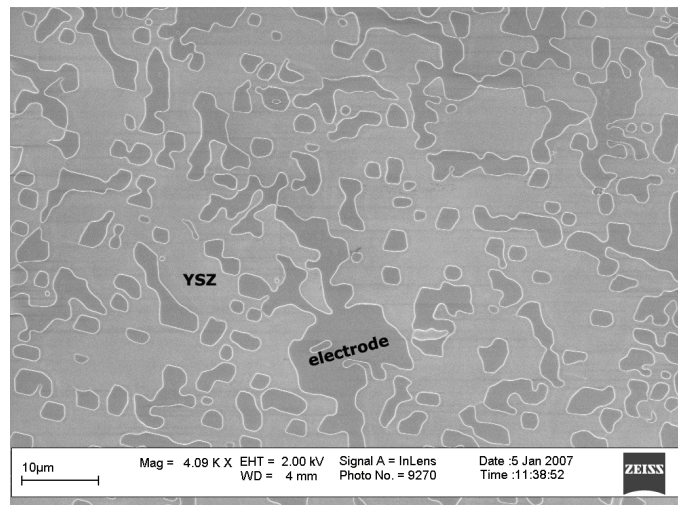


Figure 30: SEM image of sample WB39, annealed at 1200 °C for 10 hrs

5.2. Pt electrodes

An attempt is made to deposit Pt layers that have a high degree of porosity. Such layers are well suited as electrodes because of their high surface area and large number of TPBs. As discussed in paragraph 3.1.2 the influence of pressure and target-substrate on the growth of Pt films was investigated.

High porosity should be obtained at high gas pressures because gas phase particle formation will cause the deposition of larger particles with smaller kinetic energies than obtained at low pressures. The decreased mobility and increased size of the particles is expected to prevent close packing of the layer.

5.2.1. Influence of pressure and target-substrate distance on Pt films

A cross section image of the samples was made by breaking the samples and imaging the plane of fracture. The images for the depositions done at a target-substrate distance of 48 mm are shown in Figure 31. The deposition parameters can be found in 3.1.2. At deposition pressures below 1 mbar the Pt layers seem to be dense, with only a slight increase in layer thickness on increasing pressure and no change in layer structure. Above 1 mbar the deposited films become much more porous, have a lower density and become significantly rougher.

The adhesion of the deposited layer to the substrate decreases dramatically at pressures above 1 mbar. Material could be abraded even by delicate contact with a tissue or a pair of tweezers.

The influence of the target-substrate distance is shown by comparing samples deposited at equal argon pressure. This comparison is made in Figure 32, Figure 33 and Figure 34 for argon pressures of 1, 2 and 4 mbar respectively. Top view SEM images for these layers can be found in Appendix A.

All three figures show that an increase in target-substrate distance leads to an increase in porosity of the film. The thickness of the deposited layer increases with increasing target substrate distance (d_{t-s}) for 1 mbar, but decreases with increasing d_{t-s} at 2 mbar and 4 mbar.

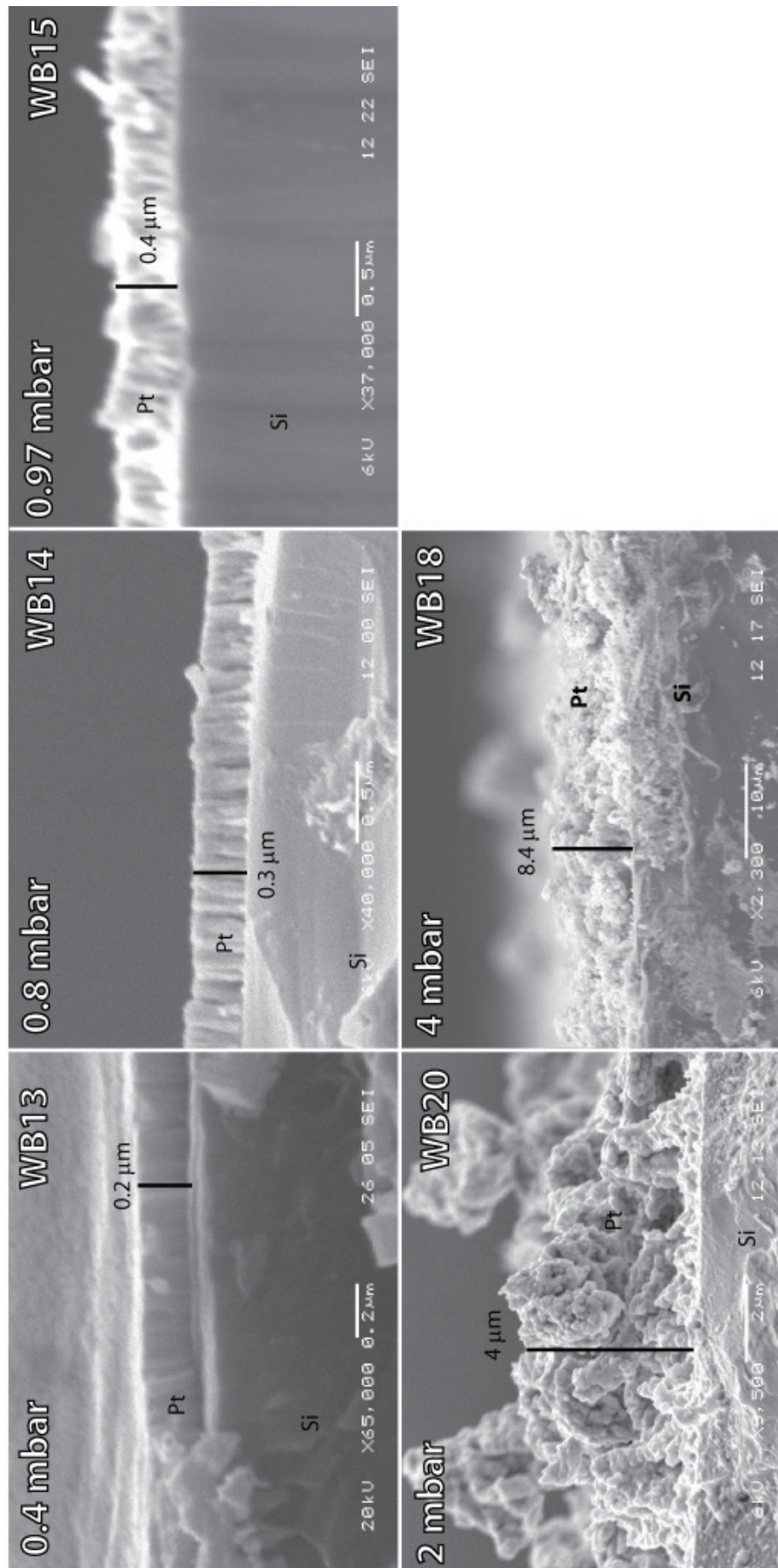


Figure 31: Pt layers deposited at 48 mm target-substrate distance with varying P_{Ar}

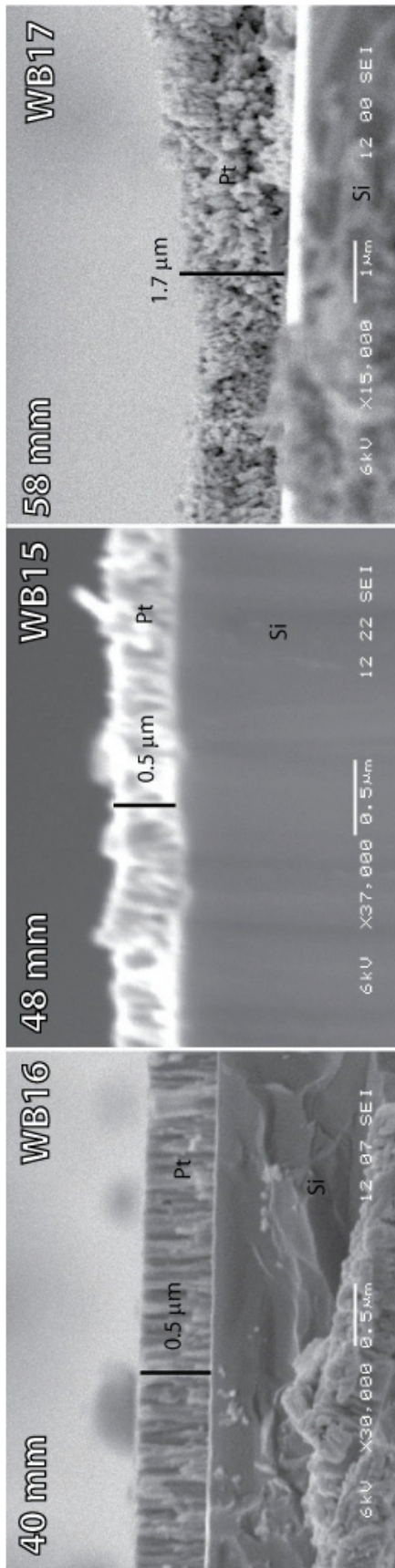


Figure 32: Pt layers deposited at 1 mbar Ar pressure at varying d_{t-s}

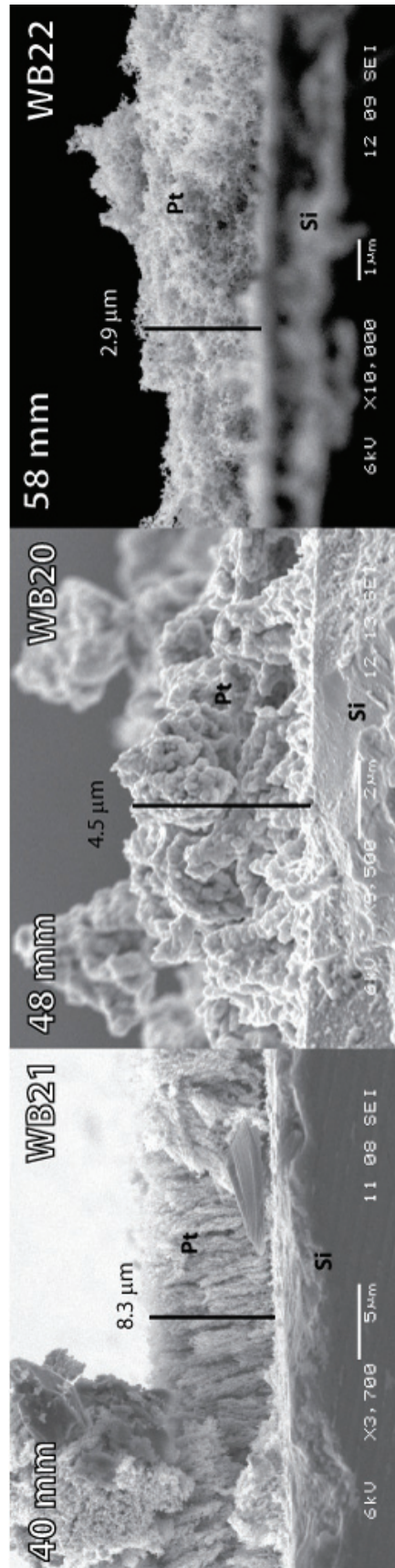


Figure 33: Pt layers deposited at 2 mbar Ar pressure at varying d_{t-s}

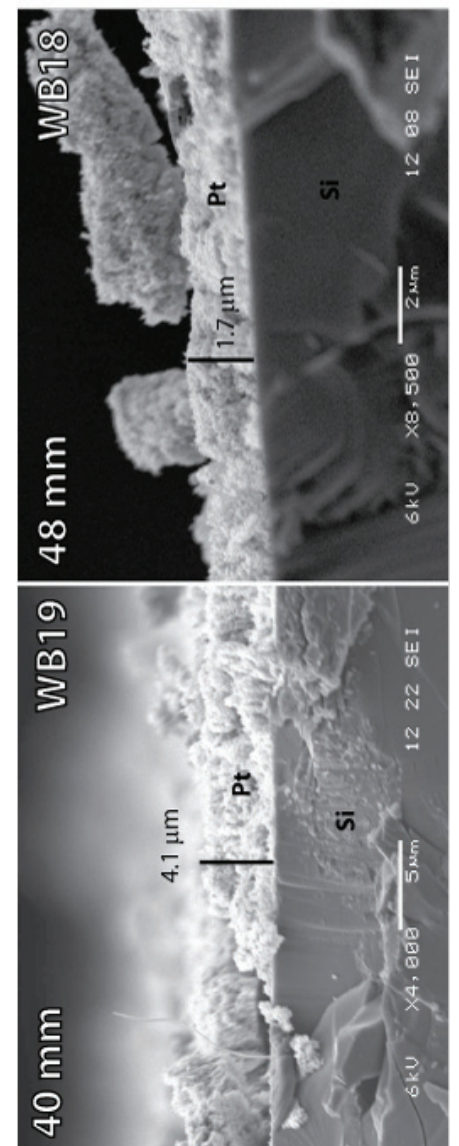


Figure 34: Pt layers deposited at 4 mbar Ar pressure at varying d_{t-s}

To investigate the thermal stability of the deposited platinum layers a sample ($d_{t-s}=58$ mm, 1 mbar Ar) was annealed in an oven at 400 °C for 4 hours, under atmospheric conditions. The SEM images taken before and after annealing are shown in Figure 35.

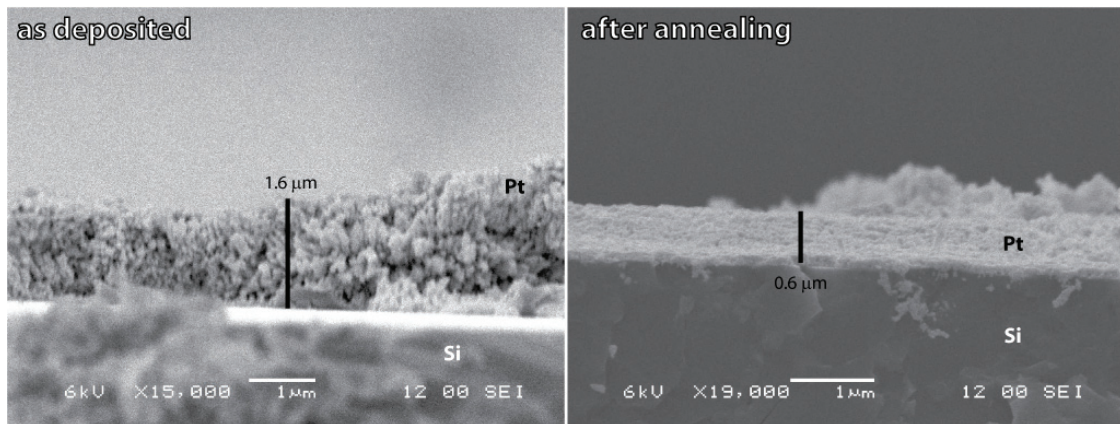


Figure 35: Sample (Pt, $d_{t-s}=58$ mm, 1 mbar Ar) before and after heating to 400 °C for 4 hrs

Figure 35 shows that the platinum layer has become thinner and more dense during annealing.

5.3. Gas flow setup

The ideal behavior for the gas flow over the sensor is a step-wise change between concentrations at the sensor surface. However, due to delay times in the MFC, finite volume of tube between MFC and sensor and mixing such a step-wise transition cannot be obtained in reality. Deviation from the ideal behavior can be characterized by two time values:

- Delay time: the time before a setpoint change results in a change of concentration
- Transition time: the time between the onset of a concentration change and reaching the maximum concentration

To be able to determine response times of the sensors it is important that the transition time from one concentration to another is significantly smaller than the response time. As indicated in paragraph 3.4.2, expected response times of the sensors range between several seconds and several minutes. Therefore, an effort is made to reduce delay and transition time to several seconds.

The gas flow setup was characterized using O_2 and N_2 . A flow of one of the gases was applied, then at $t=0$ a switch was made between the two gases, while keeping the total flow rate constant. When changing the gas from N_2 to O_2 the concentration of oxygen evolved over time as shown in Figure 36. When changing the gas flow from O_2 to N_2 the concentration profile was as shown in Figure 37. Similar experiments were done while measuring concentrations at the end of the quartz tube.

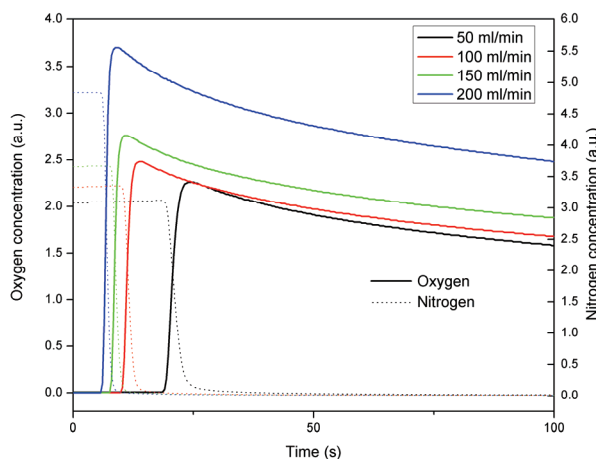


Figure 36: Concentrations of N_2 and O_2 vs. time for a transition from N_2 to O_2 at various flow rates

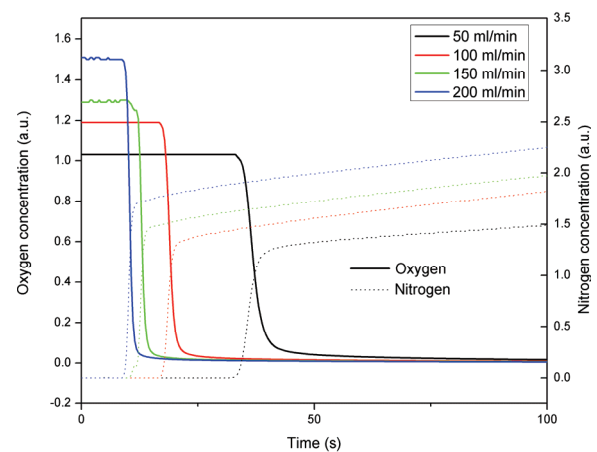


Figure 37: Concentration of N_2 and O_2 vs. time for a transition from O_2 to N_2 at various flow rates

Figure 36 shows a peak of the measured oxygen concentration after which the concentration decays to an equilibrium value. In Figure 37 it can be seen that measured nitrogen concentration continues to rise over time. The fact that in both cases the concentrations of the other gas stayed equal even though it is binary gas mixture has not been sufficiently accounted for.

5.3.1. Delay time characterization

The time delay between changes in the flow settings of the mass flow controllers (MFCs) and the gas concentrations at the beginning and at the end of the quartz tube (see Figure 13) were measured.

The time at which the oxygen concentration starts to change from its previous value is denominated t_0 . The dependence of t_0 on flow rate is shown in Figure 38.

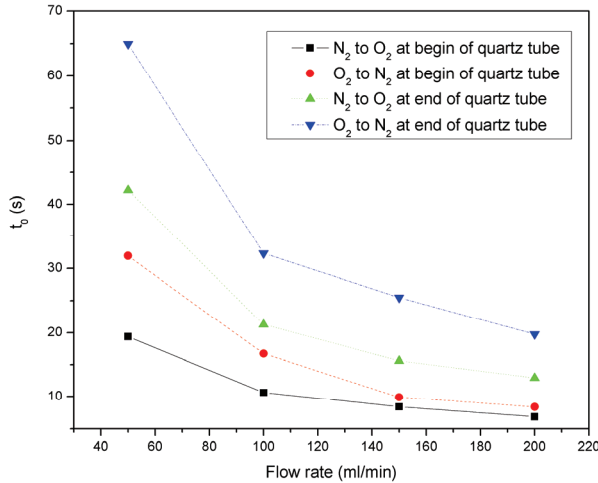


Figure 38: t_0 as a function of flow rate

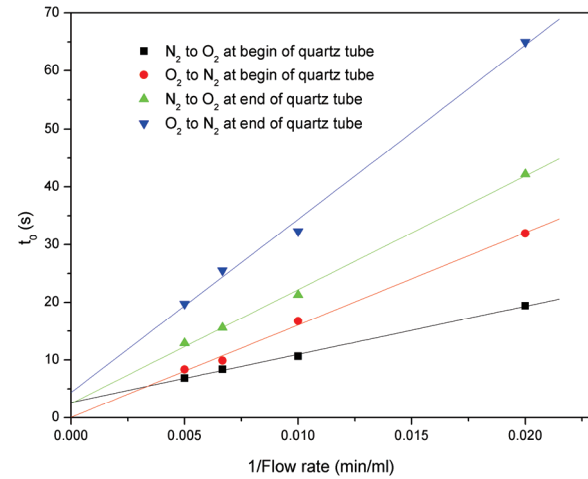


Figure 39: t_0 as a function of $1/\text{Flow rate}$

Since the volume between the MFCs and the point of measurement stays equal a first estimation for t_0 could be:

$$t_0 = t_{MFC} + t_{tube} = t_{MFC} + \frac{V_{tube}}{F} \quad (52)$$

in which t_{MFC} is the time before the MFC adjusts to the new flow rate, t_{tube} is the time required before the gas has flown through the tube to the point of measurement, V_{tube} is the volume of the tube and F is the flow rate. If equation (52) holds true then plotting t_0 as a function of $1/F$ should yield a line with a slope equal to the volume of the tube and a y-intercept equal to t_{MFC} . Calculating tube length (for a tube with inner diameter of 3.88mm) from these volumes yields lengths of the tube as recorded in Table 11. The length of tube between MFC and point of measurement was approximately 2m at the time of these measurements, which is in quite good agreement with the calculated values. This suggests that equation (52) is valid as a first estimate and suggests that a reduction in tube volume reduces delay time.

Table 11: Calculated tube length according to equation (52) for measurements at beginning of tube

Transition	Slope (cm ³)	length of tube (cm)
N ₂ -O ₂	13,9	117
O ₂ -N ₂	26,7	226

5.3.2. Transition time characterization

A second important parameter of the gas flow setup is the transition time from one gas concentration to another. The ideal behavior is a step function, but this is not a real case as can be seen from Figure 36 and Figure 37. Transition time in this case will be defined as the time from the onset of an oxygen concentration change to a new steady-state.

The transition times are recorded in Table 12 and are plotted as a function of flow rate in Figure 40

Table 12: Transition times for transitions between O₂ and N₂ at various flow rates

Flow rate (ml/min)	Transition time (s)			
	Beginning of quartz tube		End of quartz tube	
	N ₂ to O ₂	O ₂ to N ₂	N ₂ to O ₂	O ₂ to N ₂
50	5,698	9,884	20,5	53,958
100	4,176	4,547	11,407	23,554
150	3,425	4,557	9,123	16,354
200	3,415	3,045	8,362	13,679

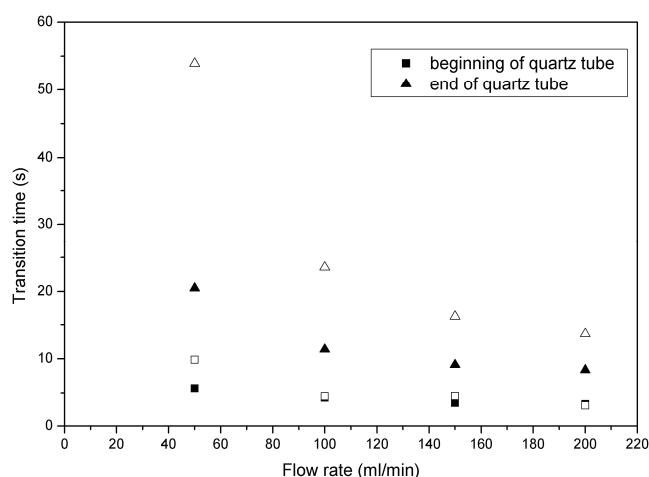


Figure 40: Transition time as a function of flow rate. Solid symbols are N₂ to O₂ transitions. Open symbols represent O₂ to N₂ transitions

Figure 40 indicates that transition times are inversely proportional to the flow rate. An increase in transition time is observed between the beginning and the end of the quartz tube as can be expected from the increase in volume and the change in tube diameter.

5.4. Sensors

5.4.1. Fabrication

Two similar O₂ sensors as well as four different NO_x sensors are fabricated. Both O₂ sensors are based on Pt sensing electrodes and Ni/NiO reference electrodes. Two of the NO_x sensors are based on this Ni/NiO reference electrode, combined with a ZnFe₂O₄ and NiO sensing electrodes respectively. The other two NO_x sensors are based on

ZnFe₂O₄ and NiO sensing electrodes respectively and Pt reference electrodes (RE) for both.

Liftoff was successfully used to pattern all the manufactured electrodes. Liftoff was also utilized to create the gold capping layers on top of the Ni/NiO electrodes but results varied. Release of the gold on top of the photoresist was troublesome and usage of ultrasonic sometimes damaged the deposited layer.

As a work-around the part of the sensor that was not to be capped was covered with a piece of Teflon tape during sputter deposition. This eliminates the problem of damaged capping layers or electrodes, but makes it more difficult to deposit a capping layer of consistent size and location. This, however, should not be a problem as long as the electrodes are not connected electrically by the capping layer and as long as the entire Ni/NiO electrode is sealed from the ambient.

5.4.2. Characterization

Sensitivity

Sensors were tested for sensitivity towards NO₂ at 600 °C by applying step wise increasing concentrations of NO₂ in a gas flow with a fixed concentration of O₂ (5%) at a fixed flow rate (150 ml/min). Results for NO_x sensor 1 (based on ZnFe₂O₄ and Pt electrodes) are shown in Figure 41. This figure shows an initial decrease of the EMF (Electro Motive Force) over time after which the EMF increases with rising NO_x concentrations. A steep decrease in EMF can be noted for an NO₂ concentration of 400 ppm, after which the EMF increases to previously recorded values.

The initial decrease in EMF can be attributed to the fact that at t=0 the flow rate was increased from zero to 150 ml/min. The decrease at 400 ppm NO₂ concentration is unexpected and should be confirmed in duplicate experiments.

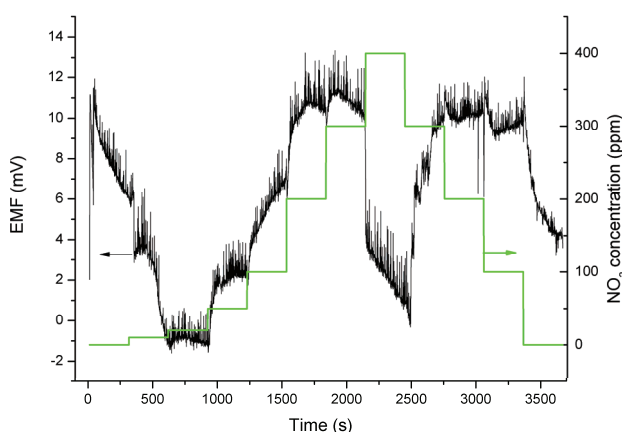


Figure 41: EMF response for NO_x sensor 1 to varying concentration of NO₂ at 600 °C as a function of time

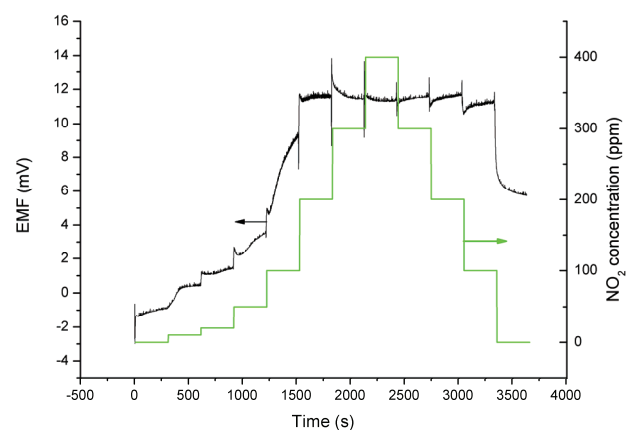


Figure 42: EMF response for NO_x sensor 2 to varying concentration of NO₂ at 600 °C as a function of time

Results for NO_x sensor 2 (based on NiO and Pt electrodes) are shown in Figure 42. An increase in NO₂ concentration shows an increase in the EMF for this sensor. However,

upon decreasing NO_2 concentration from a higher level to a previously applied concentration the EMF does not decrease to the previously recorded value within the step time.

At higher NO_2 concentrations the EMF values seem to level out for this sensor.

Sensor responses are not linear or logarithmical with respect to NO_2 concentration, as shown in Figure 43 and Figure 44 for NO_x sensor 1 and 2 respectively. EMF values were obtained by averaging the last 10 data points for a given concentration step to minimize the influence of noise. The hysteresis as discussed above can be seen for both sensors at these step times.

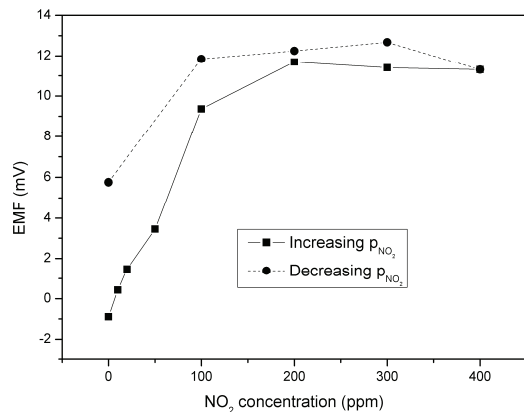


Figure 43: EMF response as function of NO_2 concentration for NO_x sensor 1 at $600\text{ }^\circ\text{C}$

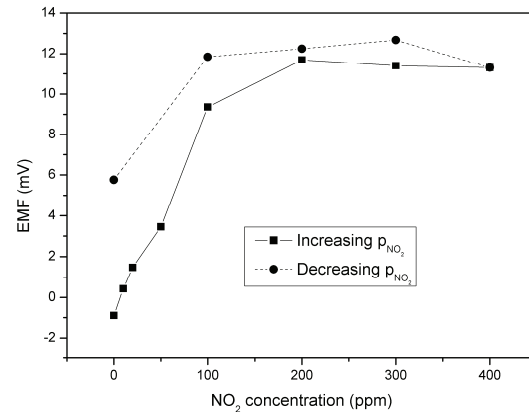


Figure 44: EMF response as function of NO_2 concentration for NO_x sensor 2 at $600\text{ }^\circ\text{C}$

Cross-sensitivity

Sensors were tested for sensitivity towards O_2 at $600\text{ }^\circ\text{C}$ by applying step wise increasing concentrations of O_2 in a gas flow with a fixed concentration of NO_2 of 200 ppm at a fixed flow rate (150 ml/min). Results for NO_x sensor 1 and 2 are shown in Figure 45 and Figure 46 respectively. The discontinuity seen in Figure 45 is unexpected and should be verified

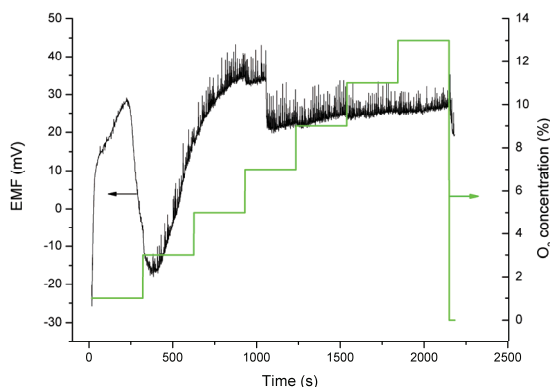


Figure 45: EMF response to changing O_2 concentrations as a function of time for NO_x sensor 1 at $600\text{ }^\circ\text{C}$

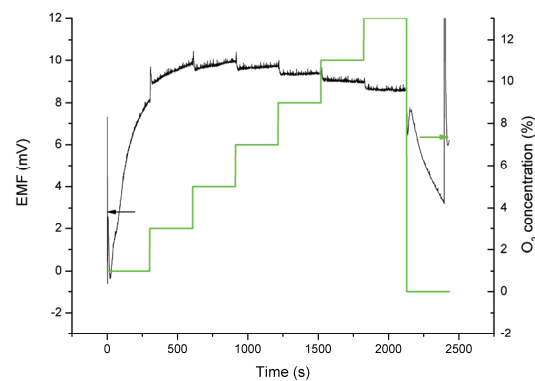


Figure 46: EMF response to changing O_2 concentrations as a function of time for NO_x sensor 2 at $600\text{ }^\circ\text{C}$

For both sensors a start-up effect of the flow can be seen. EMF response is plotted as a function of O_2 concentration in Figure 47 and Figure 48 for NO_x sensor 1 and 2 respectively. A linear fit has been made for the last 4 and 5 data points respectively.

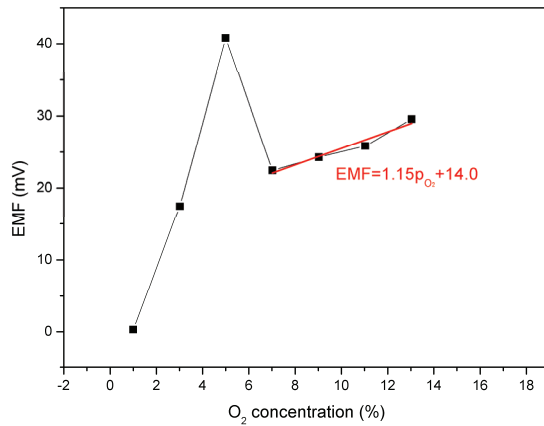


Figure 47: EMF response as function of O₂ concentration for NO_x sensor 1 at 600 °C

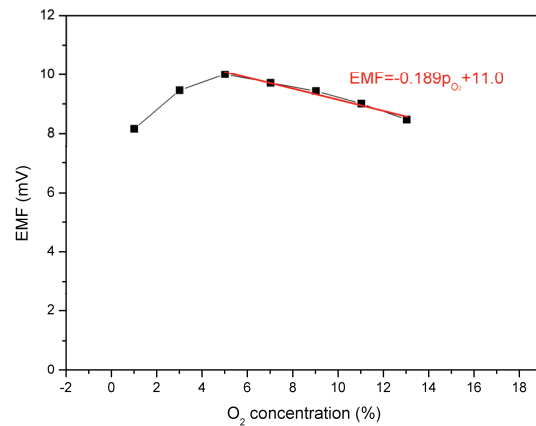


Figure 48: EMF response as function of O₂ concentration for NO_x sensor 1 at 600 °C

Response time

The response time t_{90} of a sensor is defined as the time at which 90% of the difference between the EMF value at equilibrium for the old concentration and for the new concentration. Or expressed mathematically:

$$EMF(t_{90}) = 0.9(EMF_{old}^* - EMF_{new}^*) + EMF_{old}^* \quad (53)$$

where EMF^* denotes an equilibrium value of the EMF.

For the sensitivity results shown in Figure 41 and Figure 42 it proved difficult to determine a single value for t_{90} . For NO_x sensor 2, increasing concentrations up to 200 ppm NO₂ yielded a monotonically rising response of the sensor. Further increase and subsequent decrease of the NO₂ concentrations showed a response that rose and declined over time. Values for t_{90} were extracted from this measurement for concentrations up to 200 ppm NO₂ and are plotted in Figure 49. This figure shows that no single value can be assigned to the response time of this sensor.

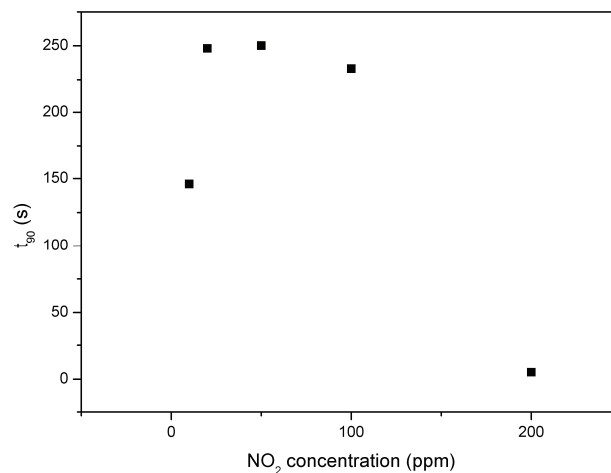


Figure 49: Response times for NO_x sensor 2, extracted from Figure 42

Response time determination for sensor 1 proved impossible due to the larger amount of noise in that measurement.

6. Discussion

In the previous chapters the experimental procedures and results were mentioned. In this chapter the results are interpreted and the consequences of these results towards building NO_x sensors are discussed.

6.1. Electrodes

The electrodes in conjunction with the electrolyte determine the sensor response. The electrolyte was not addressed in this research, but in this paragraph the results relating to the electrodes will be discussed.

6.1.1. ZnFe₂O₄ electrodes

Influence of deposition temperature on crystallinity and microstructure of ZnFe₂O₄ thin films

The Thornton zone model^[31] identifies regions of different growth behavior for sputter deposition of metals, as a function of temperature and pressure. Haghiri-Gosnet *et al* prove^[32] that this model is valid for PLD deposition of La_{0.7}Sr_{0.3}MnO₃ (LSMO) on LaAlO₃ (LAO) as well. A depiction of these regions is given in Figure 50. The temperature scale is T/T_{melt} and the pressure scale is in microns (1 micron=1 mtorr= 1.3332×10^{-3} mbar). Because a melting temperature for ZnFe₂O₄ is not known this figure can only be used qualitatively.

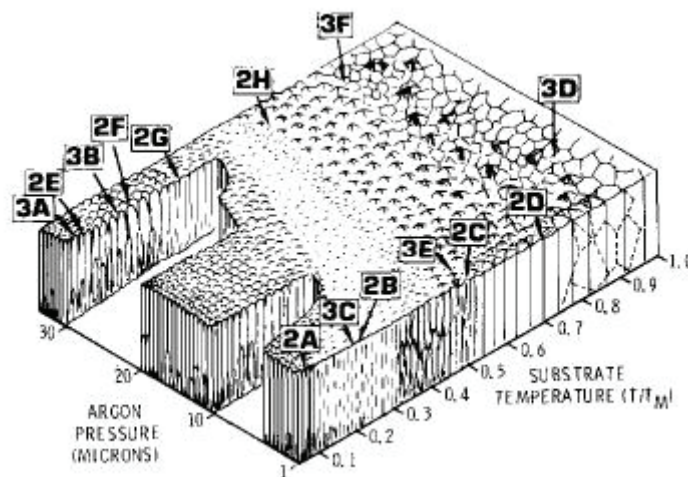


Figure 50: Development of layer structure on substrate temperature and argon pressure^[31]

The zone at low temperature is characterized by limited diffusion and random nucleation orientation. A transition zone in which surface diffusion becomes active and energetically unfavorable crystallites are eliminated is found at increasing temperatures (0.2-0.3 T/T_{melt}). These effects will occur for PLD deposited films as well. Only at

temperature above 50% of melt temperature a truly columnar structure (wider columns extending across the entire layer) is expected according to this model.

The sample deposited at 300 °C is thought to be at the lower end of the transition zone, indicated by the emergence of a cubic ZnFe_2O_4 phase and the larger, fibrous grains compared to the film deposited at 20 °C. The film deposited at 600 °C is categorized as formed at the high temperature end of the transition zone. This is indicated by larger grain sizes, smaller RMS roughness and a larger amount of cubic ZnFe_2O_4 phase. So this increasing amount of cubic phase is due to greater surface diffusion at elevated temperatures.

The fact that only {111} reflections are found for the cubic ZnFe_2O_4 phase indicates that this phase has a preferred (111) orientation on the (001) YSZ substrate, which can be due to a close match in lattice parameters. However, this should be further investigated before definite conclusions can be drawn.

Influence of annealing temperature on crystallinity and microstructure of ZnFe_2O_4 thin films

Films of ZnFe_2O_4 deposited at room temperature and annealed at 300 °C, 600 °C, 900°C for 10 hours in ambient conditions do not show any crystallinity in the XRD spectra. Sintering temperatures used in literature for ZnFe_2O_4 differ from 700 °C to 1200 °C^[33-35].

XRD analysis of a ZnFe_2O_4 film deposited at room temperature and annealed at 1200 °C for 10 hours shows the formation of Fe_2O_3 and Fe_3O_4 phases. No crystalline ZnFe_2O_4 phases were detected nor were any other phases containing Zn or Fe detected. If it is assumed that deposition was stoichiometric the conclusion must be drawn that either a Zn deficiency is developed during annealing at 1200 °C or a surplus of Zn remains in an amorphous state, undetectable by XRD.

Elemental analysis of the layers by means of X-ray Photoelectron Spectroscopy (XPS) or Energy Dispersive X-ray spectroscopy (EDX) could be used to determine which of these scenarios is true. Alternatively, the annealing could be done in a ThermoGravimetric Analysis (TGA) or Differential Scanning Calorimetry (DSC) to respectively measure weight loss and heat effects during annealing. Thirdly, annealing at intermediate temperatures could be attempted to find a temperature at which ZnFe_2O_4 is formed.

SEM and AFM analysis shows the emergence of islands after annealing at 1200 °C. This is commonly observed for porous layers and for materials with a high mobility (such as Au). In these layers the high mobility of the atoms allows diffusion to form these energetically favored islands. An increase in layer thickness should reduce or eliminate this phenomenon. However, if parameters can be tuned to yield structures with fine islands this sintering process might be employed to create finely structured electrodes.

6.1.2. Pt electrodes

Influence of pressure and target-substrate distance on Pt films

In paragraph 5.2 it was shown that the density and microstructure of Pt films grown at different gas pressures and target-substrate distances can vary significantly. Above 1 mbar the deposited layers were more porous and rough. At pressures of 1 mbar the films grew as a dense film up to a target-substrate distance of 48 mm beyond which porous films were obtained.

Increasing the gas pressure as well as increasing the distance between target and substrate reduces the kinetic energy of the ablated species reaching the substrate. This reduction in kinetic energy influences the growth of the layers in two ways: by growth of particles in the gas phase^[36] and by growth of particles on the substrate surface^[27].

An increase in d_{t-s} yields an increase in layer thickness for 1 mbar but a decrease in thickness for 2 mbar and 4 mbar. An explanation for this behavior is that there is increasing porosity upon increasing d_{t-s} , causing larger layer thicknesses at equal amounts of material deposited, but this is offset by a decrease in material deposited upon increasing d_{t-s} . Thus, a maximum in layer thickness exists

The annealing of a layer deposited at 1 mbar Ar pressure and $d_{t-s}=58$ mm for 4 hrs at 400 °C in atmospheric conditions resulted in a 60% decrease of layer height and a decrease in porosity. This is as expected, because a rise in temperature induces grain growth by increasing diffusion, leading to a sintering behavior. This reduces the porosity and thereby causes the layer to decrease in height.

The porous layers deposited in this way might be suitable as electrodes for NO_x sensors, but have a big drawback in that the adhesion to the substrate is very bad. Material could be wiped away even with a tissue. Therefore, improvements need to be made to the adhesion, before such layers are suitable as electrodes. A common solution to bad adhesion is the use of a thin intermediate adhesion layer, for which Ti is commonly used. This does not work for potentiometric sensors however, because the TPBs are essential to the sensor's operation, so it is essential that electrode and electrolyte are in direct contact. A possible solution might lie in using Pt alloys that have better adhesion to YSZ but do not diminish the sensing behavior of the electrode.

6.2. Gas flow setup

The gas flow setup had to be built to test the sensors on their sensitivity, response time and cross-sensitivity. The design considerations and the characterization of the setup are discussed in this paragraph. Characterization is done in terms of delay time and transition time. Transition time is to be lower than expected sensor response times (which are estimated to be several seconds to several minutes) to determine those response times.

6.2.1. Characterization

Figure 38 shows delay times of 10 to 40 seconds, depending on flow rate. Such a long delay time makes response time analysis of a sensor more difficult, although delay times can be compensated for if they are constant. Equation (52) was shown to be a useable first estimate for the delay time, although the difference in calculated lengths for the transition from N₂ to O₂ and vice versa cannot yet be accounted for. To reduce delay times the tube length between MFC and sensor has been reduced from 2 m to 30 cm. Delay time measurements should be repeated on the new setup.

Results in Figure 40 show a finite transition time from one gas to another, where a step function is desired. A long transition time will hinder the determination of the response time of a sensor because the effect of the transition and the sensor response become convoluted. Therefore, transition time should be minimized. The reduced pipe length in the new setup should decrease the transition time, but transition time can also be decreased by increasing flow rate. It should be noted that the transition times mentioned are worst-case scenarios, where a transition is made from 100% O₂ to 100% N₂ or vice versa. Transitions during experiments are expected to be smaller and thus the transition times are expected to be smaller.

Also, the concentrations as a function of time showed a long settling time to reach a constant value. It is thought that this is an effect caused by the mass-spectrometer. It is not certain if the used mass-spectrometer is suitable to measure high concentration of species in a gas. Also, the ion current does not seem to be a linear function of concentration of the species over the entire range. Therefore, experiments should be repeated with a different method of concentration determination, such as an oxygen sensor with a known and fast response.

6.3. Sensors

This paragraph will focus on choices made during the fabrication of the sensors and on their characterization.

6.3.1. Fabrication

In this research several sensors were fabricated, intended for O₂ or NO₂ sensing, depending on their electrode makeup. The chosen fabrication method of liftoff combined with room temperature PLD yielded electrodes with a well defined area but no crystalline structure detectable by ω -2 θ scan along the (001) direction of the substrate.

It is unknown what the effect of this absence of crystallinity on sensing behavior is. To determine this a sensor containing a ZnFe₂O₄ electrode deposited at high temperature should be made. Etching should then substitute liftoff as a patterning technique. Attempts at creating such an electrode have not been successful yet, as a residual layer was still present after etching for a time thought to correspond to the thickness of the

deposited layer. Etch rate determination should therefore be repeated, also as a function of etch time, to determine the correct etch time for a thicker layer.

The sensors fabricated in this research were all constructed with both electrodes on one side of an 8YSZ substrate that functioned as electrolyte. A planar geometry with electrodes on either side of the electrolyte is simpler to model and should therefore also be constructed, although this requires adjustments to deposition strategies and to the sample holder design.

6.3.2. Characterization

In general it can be stated that the measurement procedures for the characterization of the sensors should be revised. Currently, measurements were started at zero flow over the sample and using step times of 5 minutes. The results show a clear start-up behavior in the sensor response as a result of the transition from zero flow to the measurement flow.

Secondly it is not clear if equilibrium values of the EMF were reached during the step time. An increase in step time should be applied to ensure this.

NO_x sensor 1 and 2 (ZnFe₂O₄ and NiO sensing electrode respectively, both combined with a Pt sensing electrode) have been characterized in terms of sensitivity towards NO₂, response time and cross-sensitivity towards O₂.

Although both sensors showed a positive response to NO₂, neither had a sensitivity that could be fitted with a linear or logarithmical expression that is expected from theory. Sensitivity measurements on sensor 1 showed some unexpected behavior at 400 ppm NO₂ and should be duplicated.

A single value could not be assigned for the response time of either of the sensors, due to the large variation in response times at different concentration transitions. Also some transitions did not show a monotonic increase or decrease towards an equilibrium value, thereby making it impossible to calculate t_{90} .

Cross-sensitivity towards O₂ at 200 ppm NO₂ concentrations showed a linear dependency on O₂ concentration after start-up effects were ignored. Cross-sensitivity towards O₂ for Sensor 1 showed an increase in EMF on increasing O₂ concentration whereas sensor 2 showed a decrease in EMF on increasing O₂ concentration. A definite explanation for this difference cannot be given at this moment, but differences in catalytic behavior towards the gas phase oxidation and reduction of NO and NO₂ could play a role.

6.3.3. Considerations for commercially feasible sensors

Sensor response measurements have been executed using NO₂ in this research. However, in actual exhaust fumes a mixture of NO and NO₂ will exist. As mentioned in paragraph 2.6, the response to NO is opposite in sign to that to NO₂. Detection of total NO_x amounts without adjustments to the sensor design is therefore not possible yet. Solutions have to be developed to correlate measured EMF values to a total NO_x concentration. A possible solution could be to fully oxidize or reduce the gas mixture so that only one component reaches the sensor and is measured.

7. Conclusion

Potentiometric thin film NO_x sensors have been fabricated using PLD. Single crystal 8YSZ substrates were used as electrolyte, ZnFe₂O₄ and NiO have been used as sensing electrodes and Pt and Ni/NiO have been used as reference electrodes. Thicknesses of the electrodes were between 250 nm and 300 nm.

The optimal fluence for ZnFe₂O₄ was determined to be 3 J/cm². A deposition rate of 0.17 Å/pulse was measured for oxygen pressures from 0.04 mbar to 0.20 mbar.

ZnFe₂O₄ films were deposited at 20 °C, 300 °C and 600 °C. Films deposited at 20 °C showed no ZnFe₂O₄ crystalline phase. Films deposited at 300 °C showed columnar growth behavior and the development of a ZnFe₂O₄ phase that seems to have a (111) out of plane orientation. The layer deposited at 600 °C did not show a columnar growth and showed larger amounts of ZnFe₂O₄.

Annealing of ZnFe₂O₄ films deposited at room temperature for 10 hrs in ambient conditions was done step wise at 300 °C, 600 °C, 900 °C and 1200 °C. Up to 900 °C no difference in crystallinity was recorded and layers formed a continuous film on the substrate. After annealing at 1200 °C, phases of Fe₂O₃ and Fe₃O₄ appeared and the continuous layer had transitioned to islands on the substrate surface. During this annealing step a Zn deficiency may have been developed in the layer.

Pt layers were deposited at varying pressures (0.4 to 4 mbar) and target-substrate distances (40, 48 and 58 mm) to create porous electrodes. Above 1 mbar, layers deposited at all target-substrate distances were porous. Below 1 mbar all layers were formed as dense films. At 1 mbar the films deposited at 58 mm were porous, but at shorter distances the films were dense (as observed from SEM images).

The annealing of a porous Pt film for 4 hrs at 400 °C in atmospheric conditions resulted in a 60% decrease of layer height and a decrease in porosity.

A gas flow setup was designed and constructed. This setup is capable of supplying a gas flow composed of N₂, O₂ and NO₂ at flow rates between 0 and 200 ml/min and NO₂ concentrations between 0 and 770 ppm. Samples can be heated from room temperature to approximately 600 °C using the current method of wire bonding. The setup can be controlled using a Labview program and can perform user-defined programs of step time, flow rate and concentrations.

At a total flow rate of 150 ml/min the delay time was approximately 10s. A transition time from one O₂ to N₂ of 3.4 s was measured at a total flow rate of 150 ml/min. Pipe length between MFC and sensor has been decreased from 2 m to 20 cm to decrease the delay time.

EMF responses of NO_x sensor 1 and 2 could not be described in terms of linear or logarithmic function of NO₂ concentration, but a positive response to increasing NO₂ concentration was measured for both sensors. O₂ cross-sensitivity at 200 ppm NO₂ can be expressed as $EMF(p_{O_2}) = 1.15p_{O_2} + 14mV$ for NO_x sensor 1 and $EMF(p_{O_2}) = -0.189p_{O_2} + 11.0mV$ for NO_x sensor 2.

A single value for the response time could not be determined for either of the sensors. Values could not be compared to literature values due to this inability to quantitatively characterize the sensor's behavior.

8. Recommendations

In this chapter suggestions are made on interesting directions in which this research can be continued.

8.1. Electrodes

8.1.1. Element analysis of deposited layers

In this research XRD was utilized to characterize the deposited layers. However, XRD is a characterization technique suitable for detecting crystalline phases. Amorphous phases cannot be detected by this technique, although these might be present. Suitable techniques for element analysis of electrodes would be XPS and EDX

8.1.2. Triple phase boundaries (TPBs)

As mentioned in paragraph 2.7 the number of TPBs is thought to play an important role in sensing behavior. For thin films it is very difficult to determine the total length of the TPBs. Therefore, an interesting experiment would be the fabrication of dense film electrodes with well defined features. If films are made fully dense the length of TPB per surface area of the electrolyte can be tuned by manipulating the feature sizes (which could be made in the range of nanometers to micrometers). Correlating sensor behavior to TPB density would supply valuable information about the influence of TPBs on response time.

8.1.3. Crystallinity

The ability to grow ZnFe₂O₄ of varying amounts of crystalline phase has been shown in paragraph 5.1.4. It is uncertain if the sensor response is influenced by the crystallinity of the electrode. An interesting experiment would therefore be to correlate sensor behavior to crystallinity.

8.2. Gas flow setup

Miura *et al*^[7] have reported an decrease of response time for a tubular sensor equipped with NiO SE and Pt RE (in controlled gas environment) for a gas flow containing 5% water vapor compared to a similar gas flow without water vapor. Since water vapor is a major component of exhaust gases it would be interesting to add to the gas flow setup the ability to humidify a gas flow.

Another valuable change would be the addition of other gases that are commonly found in exhaust fumes such as CO, NO, hydrocarbons to test the cross-sensitivity of sensors to these gases.

8.3. Sensors

As mentioned in chapter 1, sensors for the automotive industry are expected to be cost-effective, durable and reliable. Not many reports on the stability of the output signal of NO_x sensors are available (notable exception is Miura *et al*^[8], who mention stability within 20% of original output signal over an 8 month period), although this severely influences the reliability of the sensors.

Investigation of signal stability over extended periods of usage in harsh conditions as found in actual exhaust fumes will be pre-requisite before such sensors can be marketed.

The effect of temperature on the EMF of the sensors has not been investigated in this research, although it is well known that it has a great influence. A more quantitative knowledge of this influence would be beneficial for sensor performance optimization.

9. References

1. Yamamoto, T., et al., *Prediction of NO_x emissions from high-temperature gas turbines: Numerical simulation for low-NO_x combustion*. *Isme International Journal Series B-Fluids and Thermal Engineering*, 2002. **45**(2): p. 221-230.
 2. Docquier, N. and S. Candel, *Combustion control and sensors: a review*. *Progress in Energy and Combustion Science*, 2002. **28**(2): p. 107-150.
 3. Zhuiykov, S. and N. Miura, *Development of zirconia-based potentiometric NO_x sensors for automotive and energy industries in the early 21st century: What are the prospects for sensors?* *Sensors and Actuators B: Chemical*. **In Press, Corrected Proof**.
 4. Dubbe, A., *Fundamentals of solid state ionic micro gas sensors*. *Sensors and Actuators B-Chemical*, 2003. **88**(2): p. 138-148.
 5. Schalwig, J., et al., *A solid-state gas sensor array for monitoring NO_x storage catalytic converters*. *Sensors and Actuators, B: Chemical*, 2004. **101**(1-2): p. 63-71.
 6. Velasco, G., J.P. Schnell, and M. Croset, *Thin solid state electrochemical gas sensors*. *Sensors and Actuators*, 1981. **2**: p. 371-384.
 7. Miura, N., et al., *High-temperature operating characteristics of mixed-potential-type NO₂ sensor based on stabilized-zirconia tube and NiO sensing electrode*. *Sensors and Actuators B-Chemical*, 2006. **114**(2): p. 903-909.
 8. Miura, N., et al., *Mixed potential type sensor using stabilized zirconia and ZnFe₂O₄ sensing electrode for NO_x detection at high temperature*. *Sensors and Actuators B-Chemical*, 2002. **83**(1-3): p. 222-229.
 9. Li, X.G. and G.M. Kale, *Influence of thickness of ITO sensing electrode film on sensing performance of planar mixed potential CO sensor*. *Sensors and Actuators B-Chemical*, 2006. **120**(1): p. 150-155.
 10. Martin, L.P., A.Q. Pham, and R.S. Glass, *Effect of Cr₂O₃ electrode morphology on the nitric oxide response of a stabilized zirconia sensor*. *Sensors and Actuators B-Chemical*, 2003. **96**(1-2): p. 53-60.
 11. Ilavsky, J. and J.K. Stalick, *Phase composition and its changes during annealing of plasma-sprayed YSZ*. *Surface and Coatings Technology*, 2000. **127**(2-3): p. 120-129.
 12. Singhal, S.C., *Advances in solid oxide fuel cell technology*. *Solid State Ionics*, 2000. **135**(1-4): p. 305-313.
 13. Kilner, J.A. and R.J. Brook, *A Study of Oxygen Ion Conductivity in Doped Nonstoichiometric Oxides*. *Solid State Ionics*, 1982. **6**(3): p. 237-252.
 14. Bouwmeester, H.J.M., *Defecten en Transport in Vaste stoffen, Studiehandleiding D3*. 2005.
 15. Miura, N., G.Y. Lu, and N. Yamazoe, *Progress in mixed-potential type devices based on solid electrolyte for sensing redox gases*. *Solid State Ionics*, 2000. **136**: p. 533-542.
 16. Fleming, W.J., *Physical Principles Governing Nonideal Behavior of Zirconia Oxygen Sensor*. *Journal of the Electrochemical Society*, 1977. **124**(1): p. 21-28.
 17. Garzon, F.H., R. Mukundan, and E.L. Brosha, *Solid-state mixed potential gas sensors: theory, experiments and challenges*. *Solid State Ionics*, 2000. **136**: p. 633-638.
-

18. *The Butler-Volmer equation*. Encyclopedia Britannica 2007 [cited 6-1-2007]; Available from: <http://www.britannica.com/eb/article-49354/electrochemical-reaction>.
 19. Fergus, J.W., *Materials for high temperature electrochemical NOx gas sensors*. Sensors and Actuators B: Chemical. **In Press, Corrected Proof**.
 20. Miura, N., et al., *Highly selective CO sensor using stabilized zirconia and a couple of oxide electrodes*. Sensors and Actuators B-Chemical, 1998. **47**(1-3): p. 84-91.
 21. Di Bartolomeo, E., M.L. Grilli, and E. Traversa, *Sensing mechanism of potentiometric gas sensors based on stabilized zirconia with oxide electrodes - Is it always mixed potential?* Journal of the Electrochemical Society, 2004. **151**(5): p. H133-H139.
 22. Zhuiykov, S., *Mathematical modelling of YSZ-based potentiometric gas sensors with oxide sensing electrodes - Part I: Model of interactions of measuring gas with sensor*. Sensors and Actuators B-Chemical, 2006. **119**(2): p. 456-465.
 23. Föll, H. *Ionic Crystals*. [cited 12-1-2007]; Available from: http://www.tf.uni-kiel.de/matwis/amat/def_en/kap_2/basics/b2_1_6.html.
 24. Webelements. *Nickel(II)Oxide*. [cited 15-1-2007]; Available from: <http://www.webelements.com/webelements/compounds/text/Ni/Ni1O1-1313991.html>.
 25. Ragone, D.V., *Thermodynamics of materials*. Vol. 1. 1995, New York: John Wiley & Sons, Inc.
 26. Kulikov, I.S., *Thermal dissociation of chemical compounds*. 1967, Jerusalem: S. Monron.
 27. Chrisey, D.B. and G.K. Hubler, *Pulsed laser deposition of thin films*. 1994, New York: Wiley-Interscience.
 28. Wikipedia. *Pulsed Laser Deposition*. 2006 [cited 24-12-2006]; Available from: http://en.wikipedia.org/wiki/Pulsed_laser_deposition.
 29. te Riele, P., *Growth of nanoparticles in the Pulsed Laser Deposition process*, in *Faculty of Science and Technology, Applied Physics*. 2004, University of Twente.
 30. MTI-corporation. *YSZ single crystals*. 2007 [cited 8-1-2007]; Available from: <http://www.mticrystal.com/datasheet/YSZ.doc>.
 31. Thornton, J.A., *Influence of apparatus geometry and deposition conditions on the structure and topography of thick sputtered coatings*. Journal of Vacuum Science and Technology, 1974. **11**(4): p. 666-670.
 32. Haghiri-Gosnet, A.M., et al., *Microstructure and magnetic properties of strained La_{0.7}Sr_{0.3}MnO₃ thin films*. Journal of Applied Physics, 2000. **88**(7): p. 4257-4264.
 33. Kurzawa, M., A. Blonska-Tabero, and I. Rychlowska-Himmel, *Phase relations in the system ZnV₂O₆-ZnFe₂O₄*. Journal of Thermal Analysis and Calorimetry, 2003. **74**(2): p. 543-547.
 34. Rigden, C.J., *Weight Losses from Zinc Ferrite and Nickel Ferrite During Sintering*. Journal of Materials Science, 1969. **4**(12): p. 1084-&.
 35. Kolta, G.A., et al., *Kinetics and Mechanism of Zinc Ferrite Formation*. Thermochemica Acta, 1980. **36**(3): p. 359-366.
 36. Lillich, H., et al., *Production and Characterization of Noble Metal Clusters by Laser Ablation*. J. Phys. Chem., 1995. **99**(33): p. 12413-12421.
-

10. List of abbreviations

Abbreviation	Page of first use	Description
PLD	1	Pulsed Laser Deposition
YSZ	9	Yttria Stabilized Zirconia
SE	10	Sensing electrode
RE	10	Reference electrode
EMF	11	ElectroMotive Force
MBE	12	Molecular Beam Epitaxy
CVD	12	Chemical Vapor Deposition
8YSZ	15	Zirconium oxide doped with 8 mol% Yttrium oxide
TPB	19	Triple Phase Boundary
AFM	31	Atomic Force Microscopy
SEM	35	Scanning Electron Microscopy
XRD	35	X-Ray Diffraction
MFC	36	Mass Flow Controller
DFD	40	Data Flow Diagram
RMS	46	Root Mean Square
XPS	62	X-ray Photoelectron Spectroscopy
EDX	62	Energy Dispersive X-ray spectroscopy
TGA	62	ThermoGravimetric Analysis
DSC	62	Differential Scanning Calorimetry

11. List of symbols

Symbol	Page of first use	Description
d_{t-s}	1	Distance from target to substrate
σ	14	Ion mobility
E_a	14	Energy of activation/Process enthalpy
T	14	Temperature
k	14	Boltzmann constant
C	14	Concentration of charge carriers
Z	14	Charge number
e	14	Charge of an electron
a_0	14	Jump distance
ν_0	14	Jump frequency
ΔS_m	14	Entropy of migration
N_0	14	Number of anion sites per unit volume
Φ	15	Electrical potential
μ	15	Chemical potential
G	16	Gibbs free energy
p_{O_2}	17	Oxygen partial pressure
j	17	Flux
L	17	Transport coefficient
D	17	Self diffusion coefficient
σ	17	Specific conductivity
i	20	Current density
α	20	Transfer coefficient
η	20	Overpotential
F	21	Faraday constant
R	24	Gas constant
a	24	Activity
t_0	54	Delay time
t_{MFC}	55	MFC switching time
t_{tube}	55	Residence time of gas in tube
V_{tube}	55	Volume of tube
t_{90}	59	Time to reach 90% of equilibrium EMF value

Appendix A: SEM images of Pt layers

